

# Temperature Structure in the Inner Regions of Protoplanetary Disks: Inefficient Accretion Heating Controlled by Nonideal Magnetohydrodynamics

SHOJI MORI,<sup>1</sup> XUE-NING BAI,<sup>2</sup> AND SATOSHI OKUZUMI<sup>3</sup>

<sup>1</sup>*Department of Earth and Planetary Sciences, Tokyo Institute of Technology, Meguro-ku, Tokyo, 152-8551, Japan; mori.s@geo.titech.ac.jp*

<sup>2</sup>*Institute for Advanced Study and Tsinghua Center for Astrophysics, Tsinghua University, Beijing 100084, China; xbai@tsinghua.edu.cn*

<sup>3</sup>*Department of Earth and Planetary Sciences, Tokyo Institute of Technology, Meguro-ku, Tokyo, 152-8551, Japan*

## ABSTRACT

The gas temperature in protoplanetary disks (PPDs) is determined by a combination of irradiation heating and accretion heating, with the latter conventionally attributed to turbulent dissipation. However, recent studies have suggested that the inner disk (a few au) is largely laminar, with accretion primarily driven by magnetized disk winds, as a result of nonideal magnetohydrodynamic (MHD) effects from weakly ionized gas, suggesting an alternative heating mechanism by Joule dissipation. We perform local stratified MHD simulations including all three nonideal MHD effects (ohmic, Hall, and ambipolar diffusion) and investigate the role of Joule heating and the resulting disk vertical temperature profiles. We find that in the inner disk, as ohmic and ambipolar diffusion strongly suppress electrical current around the midplane, Joule heating primarily occurs at several scale heights above the midplane, making the midplane temperature much lower than that with the conventional viscous heating model. Including the Hall effect, Joule heating is enhanced/reduced when the magnetic fields threading the disks are aligned/anti-aligned with the disk rotation, but it is overall ineffective. Our results further suggest that the midplane temperature in the inner PPDs is almost entirely determined by irradiation heating, unless viscous heating can trigger thermal ionization in the disk innermost region to self-sustain magnetorotational instability turbulence.

## 1. INTRODUCTION

The temperature structure of protoplanetary disks is essential for understanding many processes of planet formation. Particularly relevant is dust composition. Outside the snow line where water condenses into ice, the dust is mainly composed of water ice and silicate (Lodders 2003). The icy dust aggregates are more sticky (Wada et al. 2009) and are likely to directly grow to planetesimals via collisional sticking (Okuzumi et al. 2012; Kataoka et al. 2013), making the initial stage of planet formation proceed differently inside and outside of the snow line. Disk temperature structure is also important for understanding the water content of solar system bodies, since it directly reflects the water content of the accreted material, which is temperature sensitive. For instance, the Earth’s ocean is only 0.023 wt% of the total Earth mass, whereas the water content of comets can be as high as 50 wt% (e.g., A’Hearn et al. 2011). Similar low water content (< 5 wt%) is inferred from the TRAPPIST-1 system (Grimm et al. 2018).

The disk temperature is determined mainly by two heating mechanisms: irradiation and accretion heating. Irradiation from the central star directly heats the surface and determines the bulk disk temperature (e.g.,

Kusaka et al. 1970; Chiang & Goldreich 1997), and it generally results in a vertical temperature profile that peaks at disk surface. Accretion heating is conventionally considered to be due to viscous dissipation mediated by turbulence, a process that also drives disk accretion. It is commonly described by the Shakura-Sunyaev  $\alpha$ -disk model (Shakura & Sunyaev 1973), with effective viscosity  $\nu$  expressed as

$$\nu = \alpha c_s H, \quad (1)$$

where  $c_s$  is the sound speed,  $H = c_s/\Omega$  is the gas scale height ( $\Omega$  is the Keplerian angular velocity), and the strength of viscosity/turbulence is characterized by the dimensionless parameter  $\alpha$ . The heating rate and the viscously-driven accretion rate are then proportional to  $\alpha$  and density. With constant  $\alpha$ , heating concentrates in the disk midplane, and makes disk temperature peak at the midplane. For typical PPD accretion rate of  $\sim 10^{-8} M_\odot \text{ yr}^{-1}$  and a conventional disk model (e.g., minimum-mass solar nebula; Weidenschilling 1977; Hayashi 1981), it can be found that viscous heating dominates only at sub-AU scale, beyond which the disk temperature is mainly determined by irradiation. With higher accretion rate in early phases of disk evolution, viscous heating likely dominates to larger distances, even

up to a few 10s of AU during accretion outbursts (Cieza et al. 2016).

Turbulence in protoplanetary disks is thought to be generated mainly by the magnetorotational instability (MRI; Balbus & Hawley 1991). It occurs when the magnetic field coupled with the ionized gas is stretched by shear and rotation, and can generate strong magnetic turbulence with  $\alpha \sim 10^{-3}$ – $10^{-2}$  when the gas is well ionized (e.g., Hirose et al. 2006; Flaig et al. 2010). However, PPDs are extremely weakly ionized, and the coupling between gas and magnetic fields is substantially weakened by three non-ideal MHD effects, i.e. Ohmic diffusion, the Hall effect, and ambipolar diffusion (e.g., Wardle 2007; Bai 2011). Ohmic diffusion tends to dominate in regions where the gas density is high and the magnetic field is weak. Ambipolar diffusion tends to be important in low-density regions and relatively strong magnetic field. The Hall-dominated regime lies in between. In the inner disks, it turns out that Ohmic, Hall and ambipolar diffusion dominates in the midplane, intermediate and surface layers, respectively, and all these effects strongly affect the properties of the MRI (e.g., Jin 1996; Wardle 1999; Balbus & Terquem 2001; Desch 2004; Kunz & Balbus 2004).

Combined with the ionization conditions in PPDs, it is well known that in the inner PPD, Ohmic resistivity stabilizes the MRI around the midplane (e.g., Gammie 1996; Sano et al. 2000; Fleming & Stone 2003; Dzyurkevich et al. 2013). Without including other non-ideal MHD effects, the vigorous MRI turbulence is present only in the surface layer, leading to the picture of layered accretion. The resulting vertical temperature profile was investigated by Hirose & Turner (2011), who found lower midplane temperatures than viscous models with a constant  $\alpha$  parameter. This is because the heating by turbulent dissipation peaks at disk surface and is lost more directly by radiation cooling instead of heating the midplane.

In the recent years, however, it has been realized that ambipolar diffusion can stabilize the MRI in the upper layer of inner PPDs (e.g., Bai & Stone 2011; Gressel et al. 2015; Bai & Stone 2013; Bai 2013). With MRI fully suppressed, disk accretion and evolution is driven by magnetized disk wind (e.g., Bai 2017), whereas the non-dissipative Hall effect has more subtle behaviors that depend on the polarity of the net vertical field threading the disk (e.g., Sano & Stone 2002a,b; Kunz 2008; Lesur et al. 2014; Bai 2014, 2015; Tsukamoto et al. 2015; Simon et al. 2015; Bai & Stone 2017; Bai 2017).

In a largely laminar disk, accretion heating profile is then primarily determined by magnetic diffusivity instead of the turbulent viscosity. This heating mech-

anism is fundamentally different from viscous dissipation: there is no simple relation between heating rate and wind-driven accretion rate. The heating rate is merely related to the vertical profile of magnetic diffusivities and electric current. Therefore, detailed disk microphysics is essential to properly calculate the Joule heating rate. Furthermore, the presence of the Hall effect can amplify or reduce horizontal magnetic field depending on polarity (Lesur et al. 2014; Bai 2014, 2015; Simon et al. 2015), and is expected to yield different temperature profiles.

In this paper, we study the rate of Joule heating in the inner PPDs by means of local non-ideal MHD simulations that incorporate all three non-ideal MHD effects, calculate the resulting vertical temperature profiles, and discuss their physical implications on planet formation. The plan of this paper is as follows. In Section 2, we describe our simulation setup and model parameters. In Section 3, we present the results of our simulations for a fiducial set of parameters, focusing on the energy dissipation and temperature profiles. A parameter study is presented in Section 4, investigating when and how the accretion heating is inefficient. Limitations of our local simulations and implications on the planet formation are discussed in Section 5 before we summarize in Section 6.

## 2. METHODS AND MODEL

### 2.1. Numerical Method

We perform MHD simulations in a local shearing box (Goldreich & Lynden-Bell 1965; Hawley et al. 1995) using Athena (Stone et al. 2008), an open source MHD code based on the Godunov method with constrained transport to preserve the divergence-free condition of magnetic fields. A shearing box is centered on a fixed radius  $R_0$  and works in a frame that is corotating with its Kepler angular velocity  $\Omega$ . By ignoring disk curvature, one employs cartesian coordinates  $(x, y, z)$  for the radial, azimuthal and vertical dimensions. The orbital advection scheme (Masset 2000) described in Stone & Gardiner (2010) is used, where the velocity is decomposed into the background Kepler velocity  $\mathbf{v}_K = -(3/2)\Omega x \hat{\mathbf{y}}$  and deviation from it,  $\mathbf{v}$ . We take into account all three non-ideal MHD effects: Ohmic diffusion, the Hall effect, and ambipolar diffusion, which are characterized by diffusion coefficients  $\eta_O$ ,  $\eta_H$ , and  $\eta_A$ , respectively. We solve the following basic equations,

$$\frac{\partial \rho}{\partial t} + v_K \frac{\partial \rho}{\partial y} + \nabla \cdot (\rho \mathbf{v}) = 0, \quad (2)$$

$$\frac{\partial \rho \mathbf{v}}{\partial t} + v_K \frac{\partial \rho \mathbf{v}}{\partial y} + \nabla \cdot \left( \rho \mathbf{v} \mathbf{v} - \frac{\mathbf{B} \mathbf{B}}{4\pi} + \left( P + \frac{B^2}{8\pi} \right) \mathbf{I} \right)$$

$$= 2\Omega\rho v_y \hat{\mathbf{x}} - \frac{1}{2}\Omega\rho v_x \hat{\mathbf{y}} - \rho\Omega^2 \mathbf{z}, \quad (3)$$

$$\frac{\partial \mathbf{B}}{\partial t} = \nabla \times ((\mathbf{v}_K + \mathbf{v}) \times \mathbf{B} - c\mathbf{E}'), \quad (4)$$

where  $\rho$  is the gas density,  $\mathbf{B}$  is the magnetic field,  $\mathbf{I}$  is the identity tensor,  $P$  is the gas pressure,  $c$  is the speed of light, and  $\mathbf{E}'$  is the electric field as measured in the frame comoving with the neutral gas. The generalized Ohm's law relates  $\mathbf{E}'$  to the current density  $\mathbf{J} = (c/4\pi)\nabla \times \mathbf{B}$  as

$$\mathbf{E}' = \frac{4\pi}{c^2}(\eta_O \mathbf{J} + \eta_H \mathbf{J} \times \hat{\mathbf{B}} + \eta_A \mathbf{J}_\perp), \quad (5)$$

where  $\hat{\mathbf{B}}$  is the unit vector along the magnetic field and  $\mathbf{J}_\perp = -(\mathbf{J} \times \hat{\mathbf{B}}) \times \hat{\mathbf{B}}$  is the current density perpendicular to the magnetic field. The sign of the vertical magnetic field is taken to be positive when its direction is the same as  $\Omega$ , which is along  $\mathbf{z}$ . Note that the disk is vertically stratified by including vertical gravity  $\propto -\Omega^2 z$ . An isothermal equation of state is adopted, with  $P = \rho c_s^2$  and  $c_s$  is the isothermal sound speed. Length scales are then measured in disk scale height  $H \equiv c_s/\Omega$ . We impose the shearing periodic boundary condition for  $x$ , the periodic boundary condition for  $y$ , and the outflow boundary condition for  $z$ .

Magnetic diffusivities depend on the number densities of all charge carriers. We calculate the number densities of electrons, ions and charged grains in the disk interior, by considering ionization by cosmic rays (CR), stellar X-rays, and short-lived radionuclides, and their recombination in the gas and on dust grain's surface. The ionization prescriptions are the same as those adopted in Bai (2011), where we adopt CR ionization rate profile described in Sano et al. (2000) which is based on Umebayashi & Nakano (1981), a fitting formula in Bai & Goodman (2009) for X-ray ionization with X-ray luminosity  $L_X = 10^{30}$  ergs  $s^{-1}$  and X-ray temperature  $T_X = 5$  keV. Ionization rate by radionuclides is taken to be constant at  $7.6 \times 10^{-19}$   $s^{-1}$ . For ionization and recombination reactions, we use the same model as used in Mori & Okuzumi (2016). We represent all ion species with a single species by following Okuzumi (2009). The diffusion coefficients are expressed in terms of the Hall parameters of individual charged species as is commonly done (e.g., Wardle 2007; Bai 2011). In regimes of interest (when small dust grains are scarce), the diffusion coefficients  $\eta_O, \eta_H$ , and  $\eta_A$  can be found to be proportional to  $B^0, B^1$ , and  $B^2$  respectively, with  $f_{\text{dg}}(a/1\mu\text{m})^{-2} < 1$  (Xu & Bai 2016), where  $f_{\text{dg}}$  and  $a$  are the dust-to-gas mass ratio and radius of small dust grains, respectively. This condition is generally satisfied in PPDs with grain growth, and is marginally satisfied in the simulations presented in this study. A diffusivity table is then ob-

tained by fixing grain size, dust abundance, gas temperature, expressing  $\eta_O, Q_H \equiv \eta_H/B$  and  $Q_A \equiv \eta_A/B^2$ , as a function of gas density and ionization rate.

We also take into account the ionization by far-ultraviolet radiation (FUV) in the surface layer, where FUV can substantially enhance the level of ionization (Perez-Becker & Chiang 2011). Similar to the treatment of Bai & Stone (2013), we impose an ionization fraction of  $3 \times 10^{-5}$  in the FUV layer (from which magnetic diffusivities can be calculated), with a penetration depth of  $0.03$  g  $\text{cm}^{-2}$  to the vertical boundary. A smooth transition is imposed over a few grid cells to join the magnetic diffusivity of the bulk disk.

The importance of non-ideal MHD effects is characterized by Elsasser numbers, which read

$$\Lambda = \frac{v_A^2}{\eta_O \Omega}, \quad \chi = \frac{v_A^2}{\eta_H \Omega}, \quad \text{Am} = \frac{v_A^2}{\eta_A \Omega}, \quad (6)$$

where  $v_A = B/\sqrt{4\pi\rho}$  is the Alfvén speed. Non-ideal MHD effects are considered strong when the Elsasser numbers are around or below unity.

A mass outflow from vertical boundaries is naturally produced in our simulations that can reduce the total mass in the simulation box. To facilitate our analysis, we add mass to the system at each time step to keep this total mass unchanged to achieve steady state over long timescales. This treatment has a negligible effect on the overall dynamics.

Finally, although we aim to study the vertical temperature in disks, we still assume an isothermal equation of state in the simulations for simplicity. This is because ionization-recombination chemistry typically depends weakly on disk temperature, allowing us to reconstruct the temperature profile from the energy dissipation profile in an isothermal simulation, expecting that the dynamics is not to be strongly affected under the updated temperature profiles. In the mean time, we also perform the simulations with different isothermal temperatures in Section 5.2 to assess the validity of this approach.

## 2.2. Simulation Setup

Following Bai (2013) and Bai (2014), all our simulations are quasi-1D by using a computational domain size of  $(L_x, L_y, L_z) = (0.48H, 0.48H, 16H)$  with a computational grid of  $4 \times 4 \times 192$  cells. This is because the flow in the inner regions is expected to be largely laminar.

The initial gas density profile is taken to be a Gaussian  $\rho = \rho_0 \exp(-z^2/(2H^2))$ , where  $\rho_0$  is the initial gas density at the midplane, with initial perturbations. The amplitudes of the initial density perturbations and velocity perturbations are 1% and 0.4% of the background values, respectively. We set a density floor of  $10^{-8}\rho_0$ .

**Table 1.** Summary of the parameters

Parameter	Values	Description
$r$ [AU]	[0.2, 0.5, 1 <sup>*</sup> , 2]	Distance from the central star
$\Sigma_0$ [g cm <sup>-2</sup> ]	[170, 1700 <sup>*</sup> , 17000]	Surface density at 1 AU
$f_{\text{dg}}$	[10 <sup>-3</sup> , 10 <sup>-4</sup> <sup>*</sup> , 10 <sup>-5</sup> ]	Dust-to-gas mass ratio
$\beta_0$	[10 <sup>3</sup> , 10 <sup>4</sup> , 10 <sup>5</sup> <sup>*</sup> , 10 <sup>6</sup> ]	Initial gas-to-magnetic pressure ratio at the midplane
$\text{sgn}(B_z)$	[+1 <sup>*</sup> , -1]	Alignment of the initial magnetic field with the disk rotation axis

\*Fiducial value

The initial magnetic field configuration is given by the sum of a uniform vertical field and sinusoidal components,  $\mathbf{B}_0 = (0, B_0/\sqrt{2}\sin(\pi z/L_z), B_0)$ . The background field strength  $B_0$  is characterized by the midplane plasma beta  $\beta_0 = 8\pi\rho_0 c_s^2/B_0^2$  (the ratio of the gas pressure  $P_0 = \rho_0 c_s^2$  to the magnetic pressure at the midplane). The sign of this background vertical field can be either positive or negative, whose dynamics will be different due to the Hall effect. The sinusoidal toroidal field is included to help poloidal field grow into a physical field geometry (discussed in Section 5.1), where the field lines at upper and lower disk surface are in the opposite directions. We have confirmed that the sinusoidal component does not affect the final state.

In code units, we adopt  $H = c_s = \Omega = 1$ , and  $\rho_0 = 1$ . For magnetic field, factors of  $\sqrt{4\pi}$  are further absorbed so that magnetic pressure is simply given by  $B^2/2$  (as opposed to the equations we have written which are in cgs/Gauss units).

The magnetic diffusivities in the midplane region can become excessively large due to the extremely weak level of ionization, causing excessively small simulation timesteps. To alleviate the issue, we impose a diffusivity cap  $\eta_{\text{cap}}$  so that when the sum of all diffusivity coefficients exceeds the cap, each of them is reduced by the same factor so that its sum just reaches  $\eta_{\text{cap}}$ . In practice, we choose  $\eta_{\text{cap}} = 200c_s H$ . Note that this is much larger than the value of  $10c_s H$  that is more commonly adopted (e.g., Bai & Stone 2013; Gressel et al. 2015). Here, we choose a higher value for  $\eta_{\text{cap}}$  because we have found that convergence of main diagnostic quantities for our purposes (e.g., work done by shear) converge for  $\eta_{\text{cap}} \geq 100c_s H$ .

### 2.3. Simulation Parameters

The parameters adopted in our simulations are summarized in Table 1. Our fiducial model assumes the minimum-mass solar nebula (MMSN) model (Weiden- schilling 1977; Hayashi 1981) at 1 AU containing 0.1  $\mu\text{m}$ -sized dust grains with the dust-to-gas ratio  $f_{\text{dg}}$  of

$10^{-4}$  and the initial midplane plasma beta  $\beta_0$  of  $10^5$ . We take the fiducial value of  $f_{\text{dg}}$  to be lower than the interstellar value  $\approx 0.01$  considering the situation where most submicron-sized grains have already been incorporated into larger solid particles/bodies. As shown by Ormel & Okuzumi (2013), a reduction of  $f_{\text{dg}}$  by a factor of  $10^2$ – $10^3$  from the interstellar value best represents this situation (see also Birnstiel et al. 2011). The surface density profile is given by  $\Sigma = 1700(r/\text{AU})^{-3/2}$  g cm<sup>-2</sup>. The temperature profile of the bulk disk is set to  $T = 110(r/\text{AU})^{-3/7}$  K, following Chiang & Goldreich (1997) corresponding to a disk temperature set by stellar irradiation (the model is described in Section 3.2). This fiducial parameter set will produce the accretion rate of  $\sim 10^{-8}M_\odot \text{ yr}^{-1}$  (e.g., Bai 2014), which corresponds to PPDs around typical T Tauri stars.

The parameter sets represent inner regions ( $r = 0.2$ – $5$  AU) of young PPDs with a grain abundance corresponding to some level of grain growth. We vary the initial midplane plasma beta  $\beta_0$  from  $10^3$  to  $10^6$ , with the sign of net vertical field taken to be either positive or negative.

### 2.4. Energy Equations

Upon achieving a steady state in our isothermal simulations, we will need to analyze the energy transport in the system. In doing so, we separate total energy density  $E_{\text{tot}}$  into internal energy density  $E_{\text{int}}$ , and mechanical energy density  $E_{\text{mec}} = \rho\mathbf{v}^2/2 + \rho\Omega^2 z^2/2 + B^2/(8\pi)$ . Note that here the velocity  $\mathbf{v}$  already has Keplerian shear subtracted. As we adopt an isothermal equation of state where  $E_{\text{int}}$  does not enter self-consistently, we first focus on the equation for mechanical energy to discuss its energy balance and dissipation profiles, and then we discuss how we reconstruct the more realistic temperature profiles from the post-process simulation data.

#### 2.4.1. Dissipation Profiles

In a shearing-box, the equation of mechanical energy conservation is given by (e.g., Balbus & Hawley 1998;



Stone & Gardiner 2010)

$$\begin{aligned} \frac{\partial E_{\text{mec}}}{\partial t} + v_{\text{K}} \frac{\partial E_{\text{mec}}}{\partial y} + \nabla \cdot \mathbf{F}_{\text{mec}} \\ = -q_{\text{Joule}} + P \nabla \cdot \mathbf{v} + w_{\text{str}} \end{aligned} \quad (7)$$

where

$$\begin{aligned} \mathbf{F}_{\text{mec}} = \mathbf{v} \left( \frac{1}{2} \rho v^2 + P + \frac{1}{2} \rho \Omega^2 z^2 \right) \\ + \frac{B^2 \mathbf{v}}{4\pi} - \frac{(\mathbf{v} \cdot \mathbf{B}) \mathbf{B}}{4\pi} + \frac{c}{4\pi} \mathbf{E}' \times \mathbf{B} \end{aligned} \quad (8)$$

$$q_{\text{Joule}} \equiv \mathbf{J} \cdot \mathbf{E}' / c, \quad w_{\text{str}} \equiv \frac{3}{2} \Omega \left( \rho v_x v_y - \frac{B_x B_y}{4\pi} \right) \quad (9)$$

Here,  $\mathbf{F}_{\text{mec}}$  is the energy flux of mechanical energy, which consists of hydrodynamic (first three) and magnetic (last three) terms, respectively. The last term of  $\mathbf{F}_{\text{mec}}$ ,  $(c/4\pi) \mathbf{E}' \times \mathbf{B} = (\eta_{\text{O}} + \eta_{\text{A}}) \mathbf{J} \times \mathbf{B} - \eta_{\text{H}} B \mathbf{J}_{\perp}$ , represents the Poynting flux of non-ideal MHD effects. The term  $P \nabla \cdot \mathbf{v}$  represents the mechanical work ( $PdV$  work) done on the fluid. The term  $q_{\text{Joule}}$  represents irreversible energy dissipation by Joule heating, with the minus sign before  $q_{\text{Joule}}$  in Equation (8) meaning that this dissipation comes at the cost of mechanical energy. Of the three non-ideal MHD effects, only Ohmic and ambipolar diffusion generate heat, whereas the Hall effect is dissipationless: substituting Equation (5) into  $q_{\text{Joule}}$  gives  $q_{\text{Joule}} = (4\pi/c^2)(\eta_{\text{O}} \mathbf{J}^2 + \eta_{\text{A}} \mathbf{J}_{\perp}^2)$ . The term  $w_{\text{str}}$  represents the work done by the Reynolds and Maxwell stresses through shear, which injects mechanical energy into the system.

In our simulations, there is energy loss through the vertical boundary through a disk wind. Globally, the energy balance thus involves energy injection by  $w_{\text{str}}$ , which is then consumed by 1). Joule dissipation and 2). energy loss through  $PdV$  work and disk outflow. We emphasize that in the conventional scenario of viscously-driven accretion, the injected energy  $w_{\text{str}}$  (i.e., now being the viscous stress) is locally dissipated. However, this no longer holds in the case of wind-driven accretion. A more detailed discussion is presented in Appendix B.

#### 2.4.2. Temperature Profiles

We here use the energy dissipation profile obtained from the simulation to estimate the temperature profile. Hubeny (1990) derived the analytical formula of the temperature profile in the accretion disk with a viscosity profile. We here extend the formula by taking into account of the following points.

First, Hubeny (1990) assumed that the dissipated energy equals to the work done by the viscous stress. However, the rate profiles of the injected and dissipated energy are different, as we have discussed above. Second,

heating by stellar irradiation is known to be important in PPDs, with heating rate denoted by  $q_{\text{irr}}$ . Thus, we solve radiative transfer assuming that the net heating rate per unit volume,  $q$ , is given by the sum  $q \equiv q_{\text{Joule}} + q_{\text{irr}}$ . In addition, the dissipation profile  $q_{\text{Joule}}$  can be asymmetric about the disk midplane, thus we do not assume reflection symmetry of the  $q$  profile about the midplane as used in Hubeny (1990).

The derivation and further discussion are described in Appendix A, and the resulting temperature profile is given by

$$T(z) = \left( \frac{3\mathcal{F}_{+\infty}}{4\sigma} \right)^{1/4} \left( \tau_{\text{eff}} + \frac{1}{\sqrt{3}} + \frac{q}{3\rho\kappa_{\text{R}}\mathcal{F}_{+\infty}} \right)^{1/4}, \quad (10)$$

where

$$\begin{aligned} \tau_{\text{eff}}(z) &= \frac{1}{\mathcal{F}_{+\infty}} \int_z^{+\infty} \rho\kappa_{\text{R}} \mathcal{F}(z) dz' \\ &= \int_z^{+\infty} \rho\kappa_{\text{R}} \left( 1 - \frac{1}{\mathcal{F}_{+\infty}} \int_{z'}^{+\infty} q dz'' \right) dz', \end{aligned} \quad (11)$$

$$\mathcal{F}_{+\infty} = \frac{1}{2/\sqrt{3} + \tau_{\text{R,tot}}} \left( \frac{\Gamma}{\sqrt{3}} + \int_{-\infty}^{+\infty} \rho\kappa_{\text{R}} \left( \int_z^{+\infty} q dz' \right) dz \right) \quad (12)$$

$$\tau_{\text{R,tot}} = \int_{-\infty}^{+\infty} \rho\kappa_{\text{R}} dz \quad (13)$$

$$\Gamma = \int_{-\infty}^{+\infty} q dz. \quad (14)$$

Here,  $\kappa_{\text{R}}$  is the Rosseland mean opacity,  $\mathcal{F}_{+\infty}$  is the radiative flux at  $z = +\infty$ ,  $\Gamma$  is the total heating energy rate, and  $\sigma$  is the Stefan-Boltzmann constant. We have also assumed that the scattering coefficient is much smaller than the absorption coefficient. The effective optical depth  $\tau_{\text{eff}}$  represents the radiative-flux-weighted optical depth. Its contribution to disk temperature illustrates how disk temperature is enhanced by heat accumulation in the disk, which is crucial for understanding how accretion heating increases disk temperature.

For simplicity, throughout this work, we assume constant opacity of  $\kappa_{\text{R}} = 5(f_{\text{dg}}/0.01) \text{ cm}^2 \text{ g}^{-1}$ , which is sufficient for the demonstrative purpose on the discussion of disk heating mechanisms.

To compare the temperature profiles from our simulations with those from the conventional models, we consider the two different heating models: an “equivalent” viscous model assuming local energy dissipation, and a conventional constant- $\alpha$  viscous model.

For the equivalent viscous model, the heating profile is given by

$$q_{\text{vis}}(z) = -\frac{3\Omega}{2} \frac{B_x B_y}{4\pi}. \quad (15)$$

Note that only Maxwell stress is included because in a laminar disk wind, the Reynolds (hydrodynamic) stress is generally negligible and is also unrelated with dissipation. This model corresponds to the case where the work done by Maxwell stress is locally dissipated as if the system is turbulent. Comparison with this model will show the importance of heating profile in controlling disk temperature.

For the conventional constant- $\alpha$  model, viscosity is taken to be vertically constant given by  $\nu = \alpha c_s H$ , with viscous heating rate

$$q_{\text{vis}}(z) = \frac{9}{4} \alpha \rho c_s^2 \Omega . \quad (16)$$

The value of  $\alpha$  is set by requiring that the resulting steady-state mass accretion rate,  $\dot{M} = 3\pi\alpha\Sigma c_s H$ , matches the mass accretion rate estimated from the simulations (Bai & Stone 2013):

$$\dot{M} = \frac{2\pi}{\Omega} \int_{-z_b}^{z_b} T_{xy} dz + \frac{8\pi}{\Omega} r |T_{zy}|_{z_b} , \quad (17)$$

where  $T_{xy} = \rho v_x v_y - B_x B_y / 4\pi$  and  $T_{zy} = -B_z B_y / 4\pi$ , corresponding to contributions from radial and vertical (wind) transport of angular momentum. Here, we simply take the height of the base of the wind to be  $4H$ ,  $z_b$  (which is close to values obtained more systematically, e.g., Bai 2014).

### 3. FIDUCIAL RUN

We begin by discussing the results of the fiducial run. The outcome of the simulations is very similar to those presented in Bai & Stone (2013) and Bai (2014), where the system relaxes to a laminar state over a few tens of orbits.

We first briefly discuss the overall properties of the gas dynamics and magnetic field profiles in Section 3.1, focusing on dissipation by Joule heating. We then discuss the temperature profiles resulting from Joule heating and irradiation.

#### 3.1. Gas Dynamics and Dissipation

Figures 1 and 2 show the vertical profiles of the magnetic field, the injected and dissipated energy, the Elsasser numbers, and the energy flux, for fiducial simulations with  $B_z > 0$  and  $B_z < 0$ , respectively. The results for the same parameter set but without the Hall effect are also shown for comparison.

The overall dynamics and magnetic field profiles are largely controlled by non-ideal MHD effects. We see from the Elsasser number profiles in the bottom left panel of Figure 1 and 2 that all three non-ideal MHD effects are important within about  $z = \pm 2H$ . This results from the extremely low ionization fraction, which

strongly reduces the coupling between gas and magnetic field. The lack of charge carriers also tends to yield a flat magnetic field profile (being unable to sustain current), as seen in the corresponding top left panels. As ionization level increases, non-ideal MHD effects weaken towards the surface. Moreover, as density drops, ambipolar diffusion becomes the sole dominant effect, and remains important up to  $z \sim \pm 4.5H$  at the location of FUV ionization front. This is the key to MRI suppression in the disk surface (Bai & Stone 2013). Beyond the FUV front, the gas behaves close to the ideal MHD regime and a magnetized disk wind is launched.

#### 3.1.1. The Case of $B_z > 0$

We first discuss the  $B_z > 0$  case. On the top left panel of Figure 1, we see that horizontal components of the magnetic fields around the midplane region are strongly amplified, and is also stronger than that without the Hall effect by a factor of two. This is due to the Hall-shear instability (HSI; Kunz 2008; Lesur et al. 2014; Bai 2014). This instability simultaneously amplifies radial and toroidal fields through shear and Hall drift, creating a strong Maxwell stress.

The profile of the magnetic field is determined by non-ideal MHD effects (amplification by HSI within  $\pm 2H$  and smoothing by ambipolar diffusion) together with advection by disk winds towards the surface. The outcome is a strong vertical gradient of toroidal field  $B_y$  beyond  $\pm 2H$ . This gradient of  $B_y$  is primarily responsible for wind launching (Bai et al. 2016). In the mean time, it produces relatively strong current in the disk upper layers, and leads to the energy dissipation beyond  $z \sim \pm 2H$ . We see from the top right panel of Figure 1 that the energy dissipation rate peaks at  $z \sim \pm 3H$ . The vertically integrated dissipation rate (Equation B35), in code units, is found to be  $\Gamma_{\text{Joule}} = 2.4 \times 10^{-2}$ . This is a factor of 65 higher than the Hall-free case, which has less weaker toroidal field and its vertical gradient giving a value of  $\Gamma_{\text{Joule}} = 3.7 \times 10^{-4}$ . These values for all parameter sets are summarized in Table 2.

Energy injection is dominated by the Maxwell stress, concentrated within  $z \sim \pm 2H$  (as a result of the HSI) as shown on the upper right panel of Figure 1. The vertically integrated energy injection rate (Equation B34) reaches  $W_{\text{str}} = 3.3 \times 10^{-2}$ , much higher than the Hall-free case, which gives  $W_{\text{str}} = 2.5 \times 10^{-3}$ . From the bottom right panel of the figure, we further see that this energy is carried to upper layers first by the Poynting

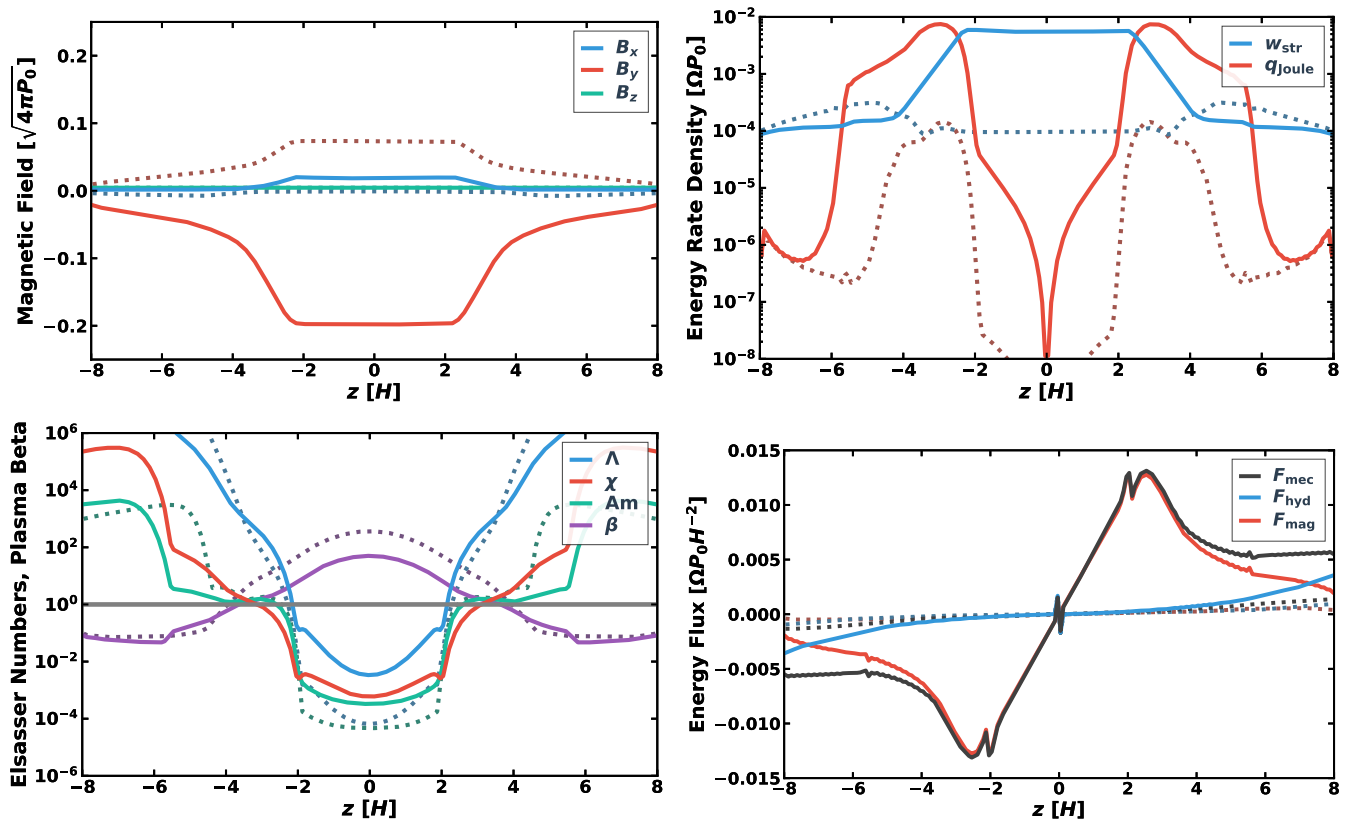


**Figure 1.** Vertical profile of magnetic fields (upper left panel), rates of energy injection and dissipation (upper right panel), the Elsasser numbers and plasma beta (lower left panel), and the energy fluxes (lower right panel). In the lower right panel,  $F_{hyd}$  and  $F_{mag}$  are the hydrodynamic and magnetic energy fluxes corresponding to the first three and last three terms, respectively, in the right-hand side of Equation (8). The solid lines are for the fiducial simulation with all non-ideal MHD effects turned on and with aligned vertical field geometry  $B_z > 0$ . The dashed lines show results from the run without the Hall effect for comparison.

flux of ambipolar diffusion,  $\eta_A \mathbf{J} \times \mathbf{B}$ , and then by advection through disk wind.<sup>1</sup>

The overall conservation of mechanical energy is achieved in the simulations. As discuss in Appendix B, part of the energy injection by Maxwell stress is dissipated into  $q_{Joule}$ , while the rest is used to drive disk winds. The division of  $w_{str}$  into the two parts depends on disk microphysics. Although the Hall effect does not generate the Joule heating, the HSI amplifies the magnetic field and hence enhances the Joule heating. The conversion of the work done by Maxwell stress into Joule heating reaches  $\sim 71\%$  for this fiducial run, as opposed to only  $\sim 15\%$  in the Hall-free run.

Finally, we comment that in this simulation, the toroidal magnetic field takes the same sign over the entire computational domain. This geometry is, however,

<sup>1</sup> There are a few spikes in the energy flux profile. The spikes at the midplane are caused by a numerical error of the gravitational potential, and the ones at  $z \sim \pm 2H$  are caused by switching on the diffusivity cap. These spikes are in very limited regions and do not affect the overall results.

unphysical for wind launching in a global disk (Bai & Stone 2013). This is a main limitation of local simulations where there is no preference of being radially inward or outward. The influence of the unphysical field geometry on the temperature profile is discussed in Section 5.1.

### 3.1.2. The Case of $B_z < 0$

While the Hall effect amplifies horizontal magnetic field when  $B_z > 0$ , it suppresses the growth of the horizontal field when  $B_z < 0$  (e.g., Bai 2014). Figure 2 shows the same as Figure 1, but for run with  $B_z < 0$ . We see that horizontal magnetic field strength is maintained at a relatively low level within  $\pm 4H$ , as compared to the Hall-free case. Consequently, the current generated by the vertical gradient of  $B_y$  is weaker, leading to much smaller Joule heating rate even compared with the Hall-free case. As a result, Joule heating is much weaker, and we find  $\Gamma_{Joule}$  to be only  $9.5 \times 10^{-6}$ .

The work done by the Maxwell stress is also significantly lower around the midplane region within  $z = \pm 2H$  (again consequence of the Hall effect suppressing

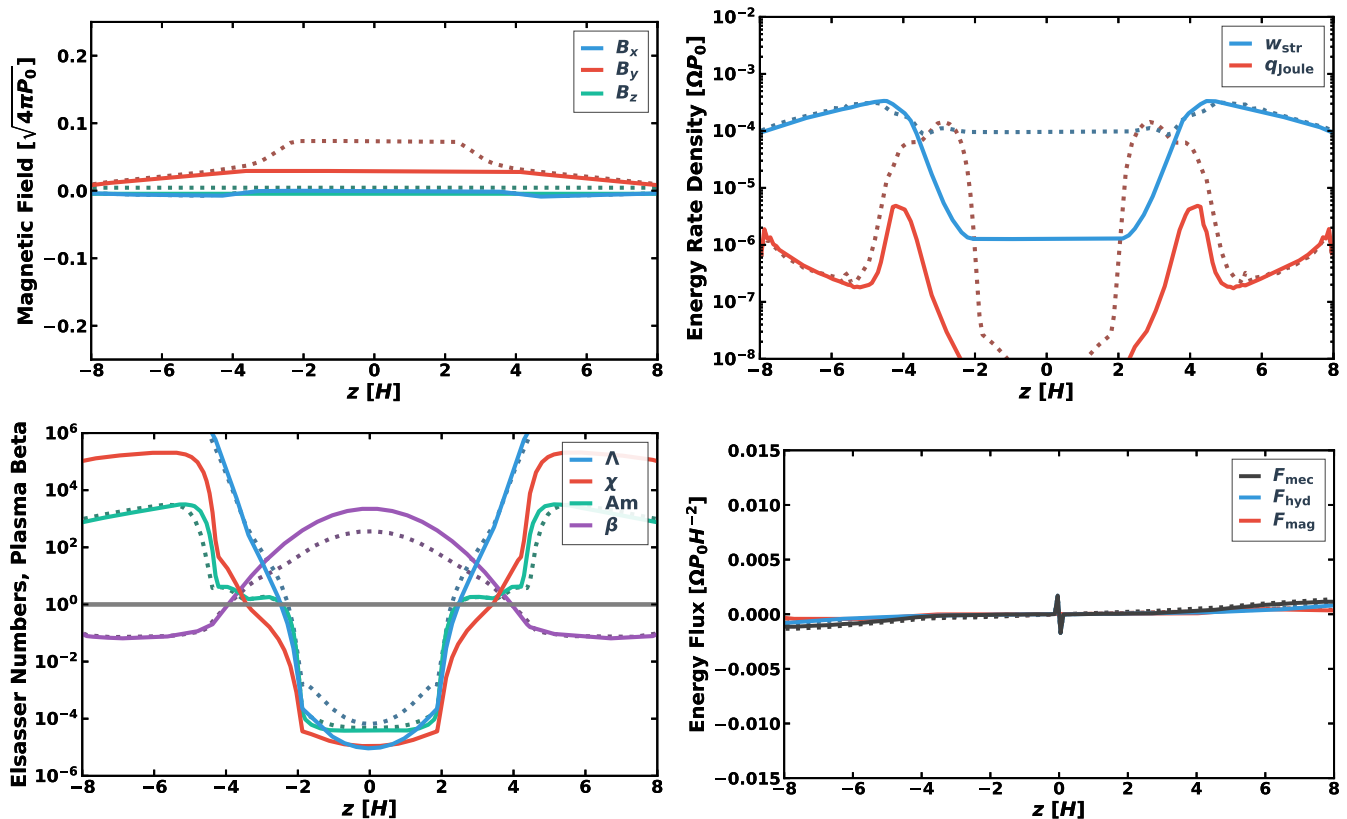


**Figure 2.** Same as Figure 1, but for the run with the anti-aligned vertical field geometry,  $B_z < 0$ .

horizontal field). Towards disk upper layers, as the Hall effect significantly weakens, we see that the magnetic field profiles are almost identical to the Hall-free case, which still yields considerable Maxwell stress, amounting to  $W_{\text{str}} = 1.9 \times 10^{-3}$ , which is associated with the wind launching process. In other words, most of the Maxwell stress is generated to assist wind launching instead of Joule dissipation.

### 3.2. Temperature Profiles

In this subsection, we reconstruct the vertical temperature profile based on the heating rate obtained earlier.

#### 3.2.1. No irradiation

First, we focus on temperature profiles determined only by the accretion heating. Without considering irradiation, the typical temperatures found in the calculations are smaller or even much smaller than the temperature assumed in our simulations. Here, we mainly focus on the comparison between different heating prescriptions (accretion heating by Joule dissipation, equivalent viscous dissipation, and constant  $\alpha$ ), and different field geometries.

Figure 3 shows that the temperature from the simulation and two viscous heating models for runs with the  $B_z > 0$  and  $B_z < 0$  cases. We also show the profile of

the effective optical depth (see Equation (11) and right panels of Figure 3), which measures the optical depth above a certain height weighted by the heating profile. The effective optical depth encapsulates the crucial differences among heating profiles. With Joule heating, and for both  $B_z > 0$  and  $B_z < 0$  cases, since the heating occurs at  $z \approx \pm 3H$  and  $\pm 4H$ , respectively, the effective optical depth no longer increases within a few scale heights. This yields relatively low temperature at the midplane region, and temperature peaks towards disk surface where most heating takes place. Overall, the temperature in the  $B_z > 0$  case is much larger than that for  $B_z < 0$ , which is largely due to the different level of total Joule dissipation controlled by the Hall effect.

In the equivalent viscous model, there is strong ( $B_z > 0$  case) and modest ( $B_z < 0$  case) energy release in the midplane region, making the effective optical depth peaking in the midplane, together with higher midplane temperatures, especially in the  $B_z > 0$  case. Temperature increases further in the surface again due to the strong Maxwell stress there.

In the constant- $\alpha$  model, the total heating rate is much higher than other models, with heating profile centrally peaked. This leads to a centrally peaked temperature profile with significantly higher midplane tem-



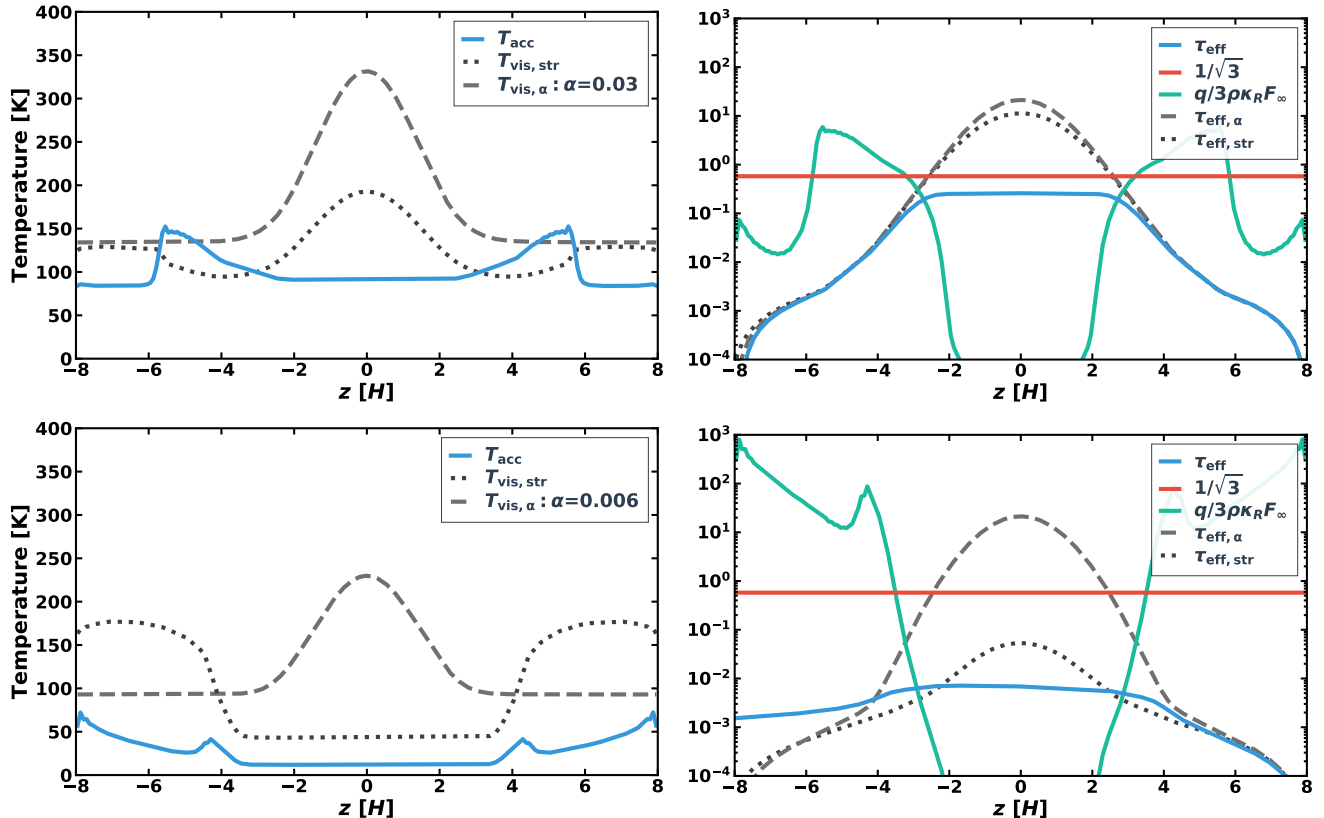


**Figure 3.** Vertical profiles of temperature (left panels) and effective optical depth (right panels) for the runs with  $B_z > 0$  (upper panels) and  $B_z < 0$  (lower panels). The solid line in the left panels shows the temperature profiles derived by using the Joule dissipation rate from the MHD simulations. The dotted and dashed lines show the temperature profiles derived from the “equivalent” viscous model,  $T_{\text{vis, str}}$ , and the ‘constant- $\alpha$ ’ model  $T_{\text{vis, } \alpha}$  (see Section 2.4.2), respectively. Irradiation heating is not included. In the right panels, the blue lines are  $\tau_{\text{eff}}$ , while the red and green lines are the second and third terms in the parentheses of Equation (10), respectively, which helps compare their relative importance in determining  $T(z)$ . The dotted and dashed lines in the right panels show the effective optical depth for the equivalent viscous model,  $\tau_{\text{eff, str}}$ , and constant- $\alpha$  model,  $\tau_{\text{eff, } \alpha}$ , respectively.

perature. Note that in the simulations, wind-driven accretion dominates in both  $B_z > 0$  and  $B_z < 0$  cases with similar total accretion rates. Therefore, in the constant- $\alpha$  model (with  $\alpha$  value chosen so that the resulting viscous accretion rate matches that from the simulations), both the effective optical depth and the resulting temperature profiles are similar in the two cases. Interestingly, despite much stronger total heating rate, the constant- $\alpha$  model generally gives surface temperatures lower than the midplane temperature, because local heating at the surface in this model diminishes as density drops.

As constant- $\alpha$  models have been widely used in the literature, the dramatic difference between the resulting temperature profiles and those obtained from our simulation results demonstrate the importance of better understanding the energy dissipation in disks. Hereafter, comparisons will be made only with the constant- $\alpha$  model.

### 3.2.2. With irradiation

We add heating energy rate  $q_{\text{irr}}$  of the stellar irradiation flux into  $q = q_{\text{Joule}} + q_{\text{irr}}$ , and then calculate the temperature profile determined by both the irradiation and Joule heating in the same way as before. In doing so, we assume that the stellar irradiation and disk thermal radiation are well-separated radiation fields in wavelength, allowing us to solve them separately (Calvet et al. 1991; Guillot 2010). The stellar irradiation flux is given by (Calvet et al. 1991)

$$\mathcal{F}_{\text{irr}}(z) = -E_0 \mu_0 \left( \exp\left(-\frac{\tau_{\text{vi}}(z)}{\mu_0}\right) + \exp\left(-\frac{\tau_{\text{vi}}(-\infty) - \tau_{\text{vi}}(z)}{\mu_0}\right) \right), \quad (18)$$

where

$$\mu_0 = r \frac{d}{dr} \left( \frac{H_p}{r} \right) \quad (19)$$

is cosine of the angle from stellar incident flux to normal of the disk surface,  $R_*$  is the stellar radius,  $H_p$  is the

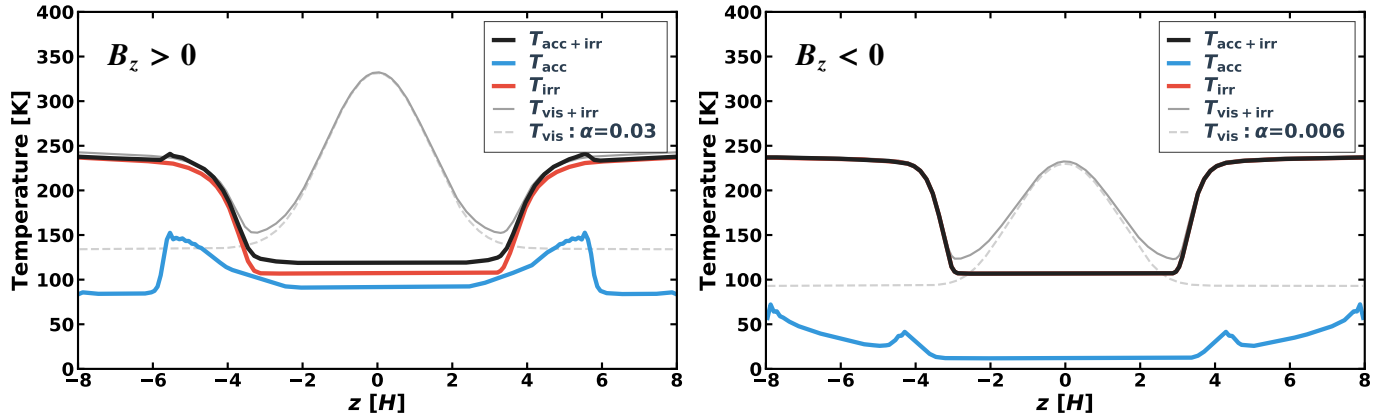


**Figure 4.** Vertical temperature profiles computed taking into account accretion heating only (blue lines), irradiation heating only (red lines), and both contributions (black lines) for the cases of  $B_z > 0$  (left panel) and  $B_z < 0$  (right panel). For comparison, the temperature profiles from the constant- $\alpha$  model with and without irradiation heating are also shown as gray solid and dashed lines, respectively.

height of the photosphere,  $E_0$  is the incoming energy flux at the disk surface, and

$$\tau_{\text{vi}}(z) = \int_z^{+\infty} \rho \kappa_{\text{vi}} dz \quad (20)$$

is the optical depth for visible light, where  $\kappa_{\text{vi}}$  is the opacity for visible light. In this paper, we assume  $\kappa_{\text{vi}} = \kappa_{\text{R}}$ . We take  $R_*$  to be the solar radius, and  $H_p$  to be  $4H$ . We also take  $E_0$  to be  $L_\odot / (8\pi r^2)$ , where we assume that stellar irradiation comes from one side of the star and  $L_\odot$  is the solar luminosity. The rate profile of heating energy of the stellar irradiation flux is then given by

$$q_{\text{irr}} = -\frac{\partial \mathcal{F}_{\text{irr}}}{\partial z} = E_0 \rho \kappa_{\text{vi}} \left( \exp\left(-\frac{\tau_{\text{vi}}(z)}{\mu_0}\right) + \exp\left(-\frac{\tau_{\text{vi}}(-\infty) - \tau_{\text{vi}}(z)}{\mu_0}\right) \right) \quad (21)$$

Figure 4 shows the temperature profiles taking into account the accretion heating (Joule heating), the irradiation heating, and the both. We find that for both  $B_z > 0$  and  $B_z < 0$  cases, the temperature profile is primarily determined by irradiation. Contribution from Joule heating is much smaller. With  $B_z > 0$  where Joule dissipation is stronger, disk midplane temperature is only enhanced by a small fraction, with additional small temperature enhancement at the surface up to about 5 scale heights where Joule dissipation profile peaks. In the case of  $B_z < 0$ , the Joule heating is so weak that its contribution to the temperature profile is largely negligible. This is in strong contrast with the constant- $\alpha$  model, where the disk midplane temperature is fully dominated by viscous heating, making midplane temperature much higher.

#### 4. PARAMETER EXPLORATION

To further access the role of accretion heating, we conduct a parameter study in this section, where we vary the gas surface density  $\Sigma$ , the initial disk magnetization (characterized by  $\beta_0$ ) and the dust-to-gas ratio  $f_{\text{dg}}$ . The results from varying  $r$ , distance to the star, is discussed separately in Section 4.1. Both signs of  $B_z$  are considered in all cases. Compared with the fiducial simulations, we only vary one parameter at a time. The range of parameters are described in Table 1, and the results are summarized in Table 2.

Figure 5 shows how the temperature profiles depend on the gas surface density. Increasing the surface density at fixed plasma  $\beta$  gives higher magnetic field strength, higher mass accretion rate, associated with stronger heating. In the mean time, it gives higher optical depth, leading to more heat accumulation. On the other hand, the ionization level decreases with higher density, which reduces current and Joule dissipation.

For accretion heating from Joule dissipation, we find that while heating and the resulting temperature profile increases with increasing surface density, its overall contribution is still relatively small compared with irradiation unless the surface density is orders of magnitude higher. Also, heating from the  $B_z > 0$  case is much stronger than the  $B_z < 0$  case, where Joule dissipation is almost always negligible compared to irradiation. For heating from the constant- $\alpha$  viscous model, higher/lower accretion rate and gas surface density (i.e., higher/lower optical depth) both yield an increase/decrease of midplane temperature, leading to large/smaller differences compared with results from the Joule heating case.

In Figure 6, we show results with different initial vertical magnetic field strength (characterized by  $\beta_0$ ) in a way similar to Figure 5. Obviously, stronger/weaker net vertical field gives higher/lower accretion rate (largely

**Table 2.** Summary of the results for all parameter sets

$r$ [AU]	$\Sigma$ [g/cm <sup>2</sup> ]	$\beta_0$	$f_{\text{dg}}$	$\alpha_r$	$\alpha_z$	$\dot{M}_r$ [M <sub>⊙</sub> /yr]	$\dot{M}_z$ [M <sub>⊙</sub> /yr]	$W_{\text{str}}$	$\Gamma_{\text{Joule}}$	$\Gamma_{\text{acc}}$	$T_{\text{acc}}$ [K]	$T_{\text{vis}}$ [K]	$T_{\text{irr}}$ [K]
1	1700	1e5	1e-4	1.1e-2	1.6e-2	5.7e-8	8.0e-8	3.3e-2	2.4e-2	1.5e-1	91	330	105
1	1700	1e5*	1e-4	2.9e-4	7.3e-3	1.4e-9	3.6e-8	2.5e-3	3.7e-4	4.3e-2	32	239	105
1	1700	-1e5	1e-4	5.5e-5	6.4e-3	2.7e-10	3.2e-8	1.9e-3	9.5e-6	3.6e-2	12	229	105
1	17000	1e5	1e-4	4.5e-3	1.2e-2	2.3e-7	5.9e-7	1.4e-2	9.3e-3	9.3e-2	135	911	106
1	17000	-1e5	1e-4	1.2e-6	2.6e-3	6.1e-11	1.3e-7	5.5e-4	3.8e-5	1.5e-2	32	573	105
1	170	1e5	1e-4	1.8e-2	2.4e-2	9.2e-9	1.2e-8	5.4e-2	3.6e-2	2.4e-1	56	124	105
1	170	-1e5	1e-4	7.7e-4	1.2e-2	3.8e-10	6.1e-9	7.0e-3	7.2e-4	7.3e-2	20	92	105
1	17	1e5	1e-4	1.0e-2	5.4e-2	5.0e-10	2.7e-9	3.9e-2	9.9e-3	3.6e-1	23	67	106
1	17	-1e5	1e-4	6.3e-3	3.8e-3	3.2e-10	1.9e-10	6.0e-2	7.4e-3	5.7e-2	20	42	106
2.0	601	1e5	1e-4	1.2e-2	1.4e-2	4.5e-8	5.1e-8	3.5e-2	2.4e-2	1.5e-1	51	140	78
2.0	601	-1e5	1e-4	9.1e-4	2.5e-2	3.4e-9	9.3e-8	1.1e-2	4.2e-3	1.5e-1	33	140	77
0.5	4808	1e5	1e-4	1.0e-2	2.1e-2	6.7e-8	1.4e-7	3.0e-2	2.1e-2	1.7e-1	162	793	146
0.5	4808	-1e5	1e-4	3.8e-5	5.8e-3	2.5e-10	3.9e-8	1.3e-3	2.5e-5	3.3e-2	27	524	146
0.2	19007	1e5	1e-4	7.4e-3	2.9e-2	7.3e-8	2.9e-7	2.3e-2	1.5e-2	2.0e-1	340	2549	235
0.2	19007	-1e5	1e-4	1.6e-6	4.2e-3	1.6e-11	4.2e-8	5.9e-4	5.2e-5	2.4e-2	77	1492	235
1	1700	1e6	1e-4	3.6e-3	3.6e-3	1.8e-8	1.8e-8	1.0e-2	7.5e-3	4.1e-2	68	236	105
1	1700	-1e6	1e-4	5.8e-5	9.0e-4	2.9e-10	4.5e-9	9.6e-4	3.2e-5	5.4e-3	17	142	105
1	1700	1e4	1e-4	3.3e-2	7.6e-2	1.6e-7	3.8e-7	1.0e-1	6.6e-2	6.1e-1	118	465	106
1	1700	-1e4	1e-4	3.3e-4	2.2e-2	1.6e-9	1.1e-7	6.3e-3	3.9e-4	1.3e-1	30	313	105
1	1700	1e3	1e-4	8.8e-2	3.8e-1	4.4e-7	1.9e-6	3.0e-1	1.8e-1	2.6	152	670	106
1	1700	-1e3	1e-4	5.8e-3	9.0e-2	2.9e-8	4.5e-7	3.3e-2	1.7e-2	5.4e-1	77	451	105
1	1700	1e5	1e-3	4.1e-3	1.3e-2	2.0e-8	6.2e-8	1.3e-2	7.2e-3	9.4e-2	81	514	106
1	1700	-1e5	1e-3	5.4e-5	6.4e-3	2.7e-10	3.2e-8	1.9e-3	9.5e-6	3.6e-2	12	405	105
1	1700	1e5	1e-5	1.9e-2	1.8e-2	9.4e-8	9.2e-8	5.4e-2	4.1e-2	2.1e-1	97	213	105
1	1700	-1e5	1e-5	5.3e-5	6.4e-3	2.6e-10	3.2e-8	1.9e-3	9.4e-6	3.6e-2	12	138	105

\* Run without Hall effect.

NOTE— The sign of  $\beta_0$  express the sign of  $B_z$ . The accretion rates  $\dot{M}_r$  and  $\dot{M}_z$  are calculated by the first and second terms of Equation (17), respectively. The alpha value  $\alpha_r$  and  $\alpha_z$  are the equivalent viscous  $\alpha$  values to yield accretion rates of  $\dot{M}_r$  and  $\dot{M}_z$ , respectively. The energy production rate  $W_{\text{str}}$ ,  $\Gamma_{\text{Joule}}$ , and  $\Gamma_{\text{acc}}$  are given by the integration of the work done by the stress  $w_{\text{str}}$ , Joule dissipation rate  $q_{\text{Joule}}$ , and the energy dissipation rate in the constant- $\alpha$  model to yield total accretion rate  $\dot{M}_r + \dot{M}_z$ . The temperatures  $T_{\text{acc}}$ ,  $T_{\text{vis}}$ , and  $T_{\text{irr}}$  are the midplane temperatures given by the Joule heating, viscous heating of the expected mass accretion rate (from the constant- $\alpha$  model), and irradiation heating, respectively.

wind-driven). We find that the variation of  $\beta_0$  and does not strongly alter the location of Joule dissipation. Increasing/decreasing the field strength mainly enhances/reduces the total rate of Joule dissipation. The change in dissipation is more significant for the  $B_z > 0$  case, causing appreciable changes in midplane and surface temperatures, whereas in the  $B_z < 0$  case, disk temperature profile is again almost entirely determined by irradiation. In the constant- $\alpha$  model, again, the midplane temperature is dominated by viscous dissipation and is sensitive to changes in accretion rate.

We then discuss the dependence of dust abundance in Figure 7 by varying the dust-to-gas mass ratio of  $10^{-3}$  and  $10^{-5}$ . The dust abundance affects the ionization fraction and optical depth. Higher dust abundance leads to higher the optical depth. It makes the optically thick region more extended (as seen in the  $T_{\text{irr}}$  profile), more

heat accumulation, and hence higher midplane temperature. In the mean time, it leads to lower ionization fraction. This acts to suppress field growth, making dissipation take place at higher altitude, and hence reduce the contribution from Joule heating. For lower dust abundance, lower optical depth tends to reduce midplane temperature, whereas the higher ionization fraction enhances Joule dissipation especially towards the surface (the disk remains laminar in our simulation), as well as its overall contribution to disk heating. We thus see prominent temperature bumps at disk surface in the  $B_z > 0$  case. For field polarities, lower grain abundance gives higher surface temperature.

#### 4.1. Dependence on Radial Distance

In Figure 8, we discuss the dependence of accretion heating on the distance from the star,  $r$ . We first discuss

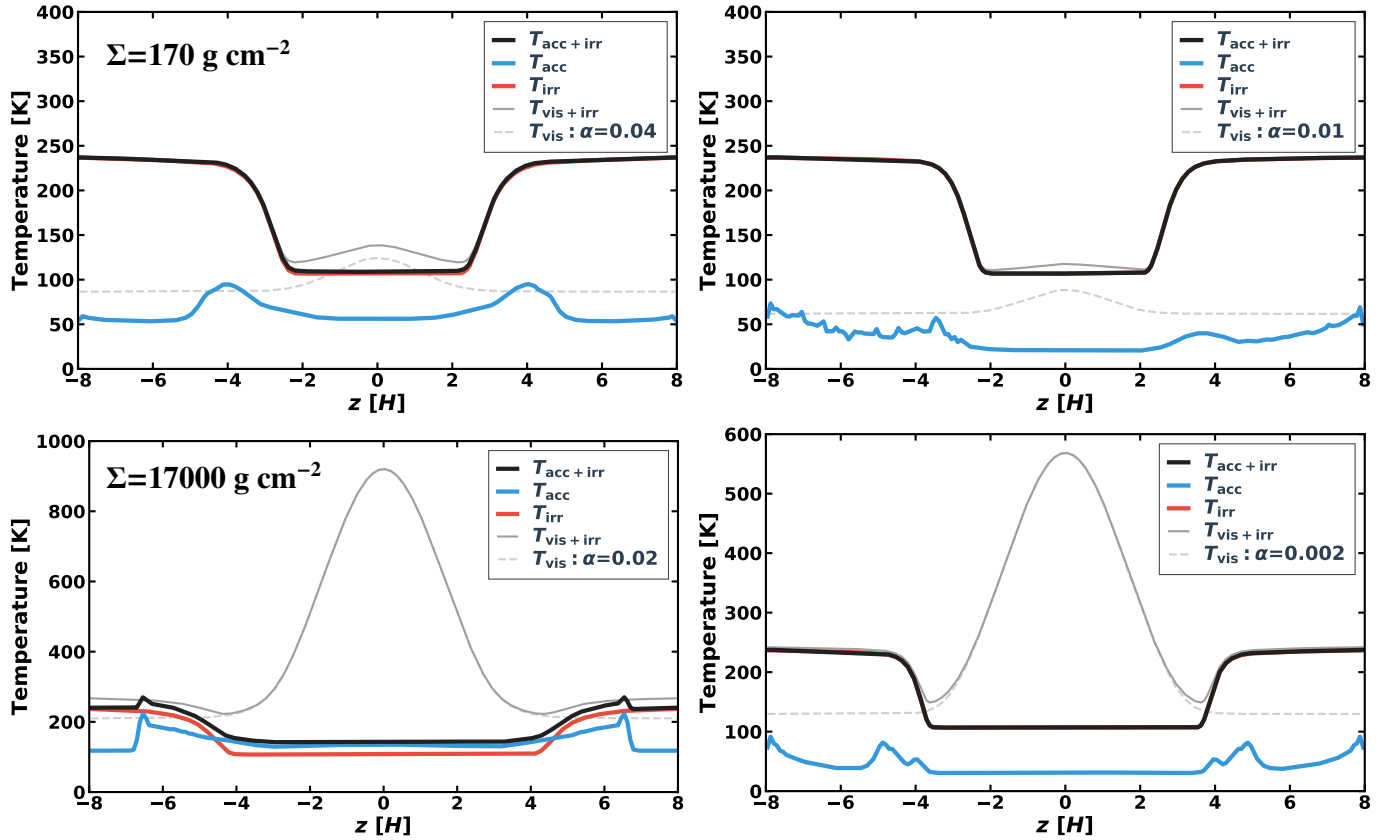


**Figure 5.** Same as Figure 4, but for runs with  $\Sigma = 170$  (top) and  $17000 \text{ g cm}^{-2}$  (bottom) and with  $B_z > 0$  (left) and  $B_z < 0$  (right). Note that the scales in some figures are different.

the scenario from the conventional constant- $\alpha$  viscously-driven accretion model. Towards larger distance, while irradiation gets weaker, it tends to play a more dominant role because viscous heating decreases with distance even faster. This is evident in our calculations assuming viscous heating with constant  $\alpha$  parameters. Towards smaller  $r$ , we see that within  $r \lesssim 0.5 \text{ AU}$ , midplane temperature reaches and exceeds  $\sim 800\text{K}$  in the constant- $\alpha$  model, which would trigger thermal ionization of Alkali species, and likely make the midplane region MRI active (Desch & Turner 2015). This implies that MRI turbulence can be self-sustained in this region: viscous dissipation from the MRI maintains high midplane temperature needed for thermal ionization to sustain the MRI.

In the framework of our simulations (where disk temperature is fixed to irradiation temperature), the same trend holds in the case of  $B_z > 0$  in the sense that the role of Joule dissipation becomes more important towards smaller distances, and start to dominate over at  $r \lesssim 0.5 \text{ AU}$ . For the  $B_z < 0$  case, however, even at a close distance of  $r = 0.2 \text{ AU}$ , Joule dissipation is still negligible compared with irradiation heating. In both cases, the system temperature never gets close to

$\sim 800\text{K}$ , the rough threshold for thermal ionization<sup>2</sup>, and in the simulations, the systems are well in the laminar state. This means that the laminar states from our simulations are equally valid solutions, in addition to the case self-sustained MRI turbulence discussed earlier. Whether the system can stay in one case or the other then must be determined from global conditions and/or evolution history.

In reality, the innermost disk region (or more to the extreme, inner rim directly illuminated by the star) is likely warm enough to be MRI turbulent, which must be separated from a cooler laminar region somewhere further out. This interface has been conventionally designated as the inner dead zone boundary. Previous numerical studies already found it to be highly dynamic (e.g., Faure et al. 2014; Flock et al. 2017), though only Ohmic resistivity was considered and angular momentum transport/Joule heating from a disk wind was absent. Our result further suggests that this boundary should also be accompanied with abrupt temperature

<sup>2</sup> Note that thermal ionization of alkali species is not included in our ionization chemistry model, and it is not needed as the results show.

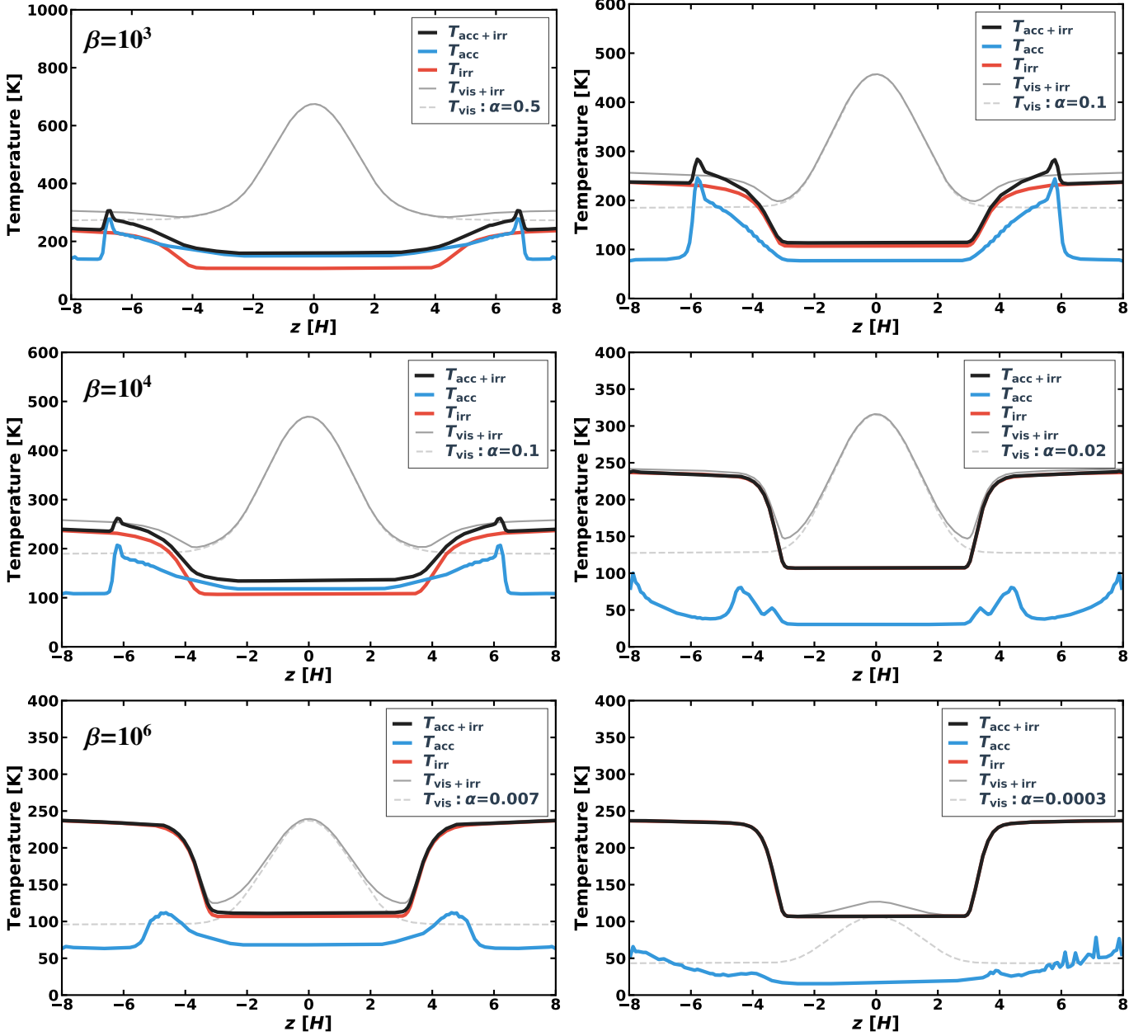


Figure 6. Same as Figure 5, but for runs with  $\beta = 10^3, 10^4$ , and  $10^6$  (from top to bottom).

transitions, which may further complicate its dynamics, with potentially important implications on planet formation in this region.

## 5. DISCUSSION

### 5.1. Geometry of Magnetic Field

We have employed local shearing-box simulations to study the vertical distribution of current density. One important issue of this approach is that a horizontal current layer that accompanies a flip of the sign of the horizontal magnetic field (which is necessary for a physical field geometry in a disk wind) tends to be unstable in

shearing-box simulations as pointed out by Bai & Stone (2013). They found that the natural geometry of global magnetic field in a shearing box is such that the field lines have no flip and the horizontal fields on the top and bottom sides of the box have the same direction. This tendency is also observed in our simulations: even though we start with magnetic field geometry of a flip at the midplane, the flip gradually moves toward high altitude and eventually escapes from the simulation box through the vertical boundary. The instability of the horizontal current layer seems to occur because the field



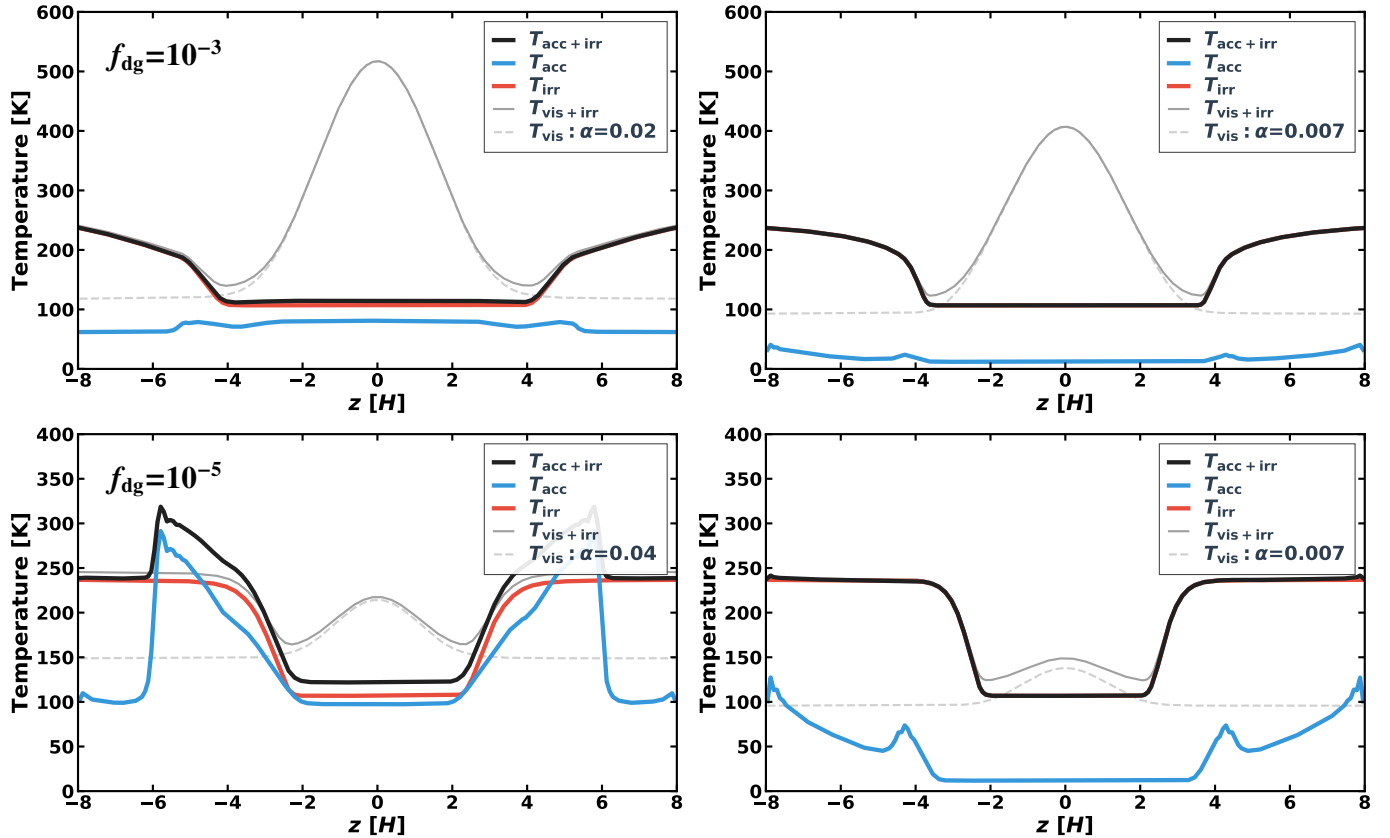


Figure 7. Same as Figure 5, but for runs with  $f_{dg} = 10^{-3}$ , and  $10^{-5}$  (from top to bottom).

lines straighten out under magnetic tension that is amplified by the Keplerian shear and the Hall effect.

In reality, the magnetic field threading a protoplanetary disk should have global geometry such that the field lines are directing outward on both side of the disk, and hence the horizontal field should have a flip at some height within the disk. Depending on its height, the current layer accompanied by this flip could contribute to the heating of the disk interior, but this cannot be evaluated in our local simulations.

Recent global simulations by Bai (2017) that include all three non-ideal MHD effects found that the flip occur naturally in global simulations. In particular, in their fiducial model with parameters similar to ours, thanks to the Hall effect, the flip occurs at very high altitude (about  $4\text{--}5H$  above the midplane) on one side of the disk in the inner disk (a few AU). The location of the flip roughly coincides with the location of the FUV front. Because of such high altitude, magnetic field profiles in the bulk disk below the location of the flip are in fact similar to the profiles obtained in shearing-box. Therefore, on the one hand, our calculations miss additional heating resulting from the strong current layer due to the flip. On the other hand, this single-sided heating at very high altitude likely only causes very localized

heating near the disk atmosphere (see Figure 10 in Appendix A for an example), and has very limited impact to the disk midplane temperature. Meanwhile, we plan to address this issue further with global simulations in future works.

## 5.2. Dependence on the Prior Temperature

The approach we have taken to study disk heating is not self-consistent: although the temperature profiles obtained using Equation (10) properly take into account Joule heating and irradiation heating, the Joule heating rates are obtained from isothermal MHD simulations. For this reason, the “posterior” temperature obtained from Equation (10) differs from the “prior” temperature given in the MHD simulations. Although self-consistent modeling will be the subject of our future work, it is important to clarify within the current approach how much a variation of the prior temperature can influence the resulting heating rate and posterior temperature.

For this purpose, we repeated the fiducial run but with a prior temperature of  $T = 280$  K, which is approximately twice the fiducial value. This choice is motivated by the fact that for passively irradiated disks, the temperature in the optically thin surface region is about two times higher than that in the optically thick disk interior

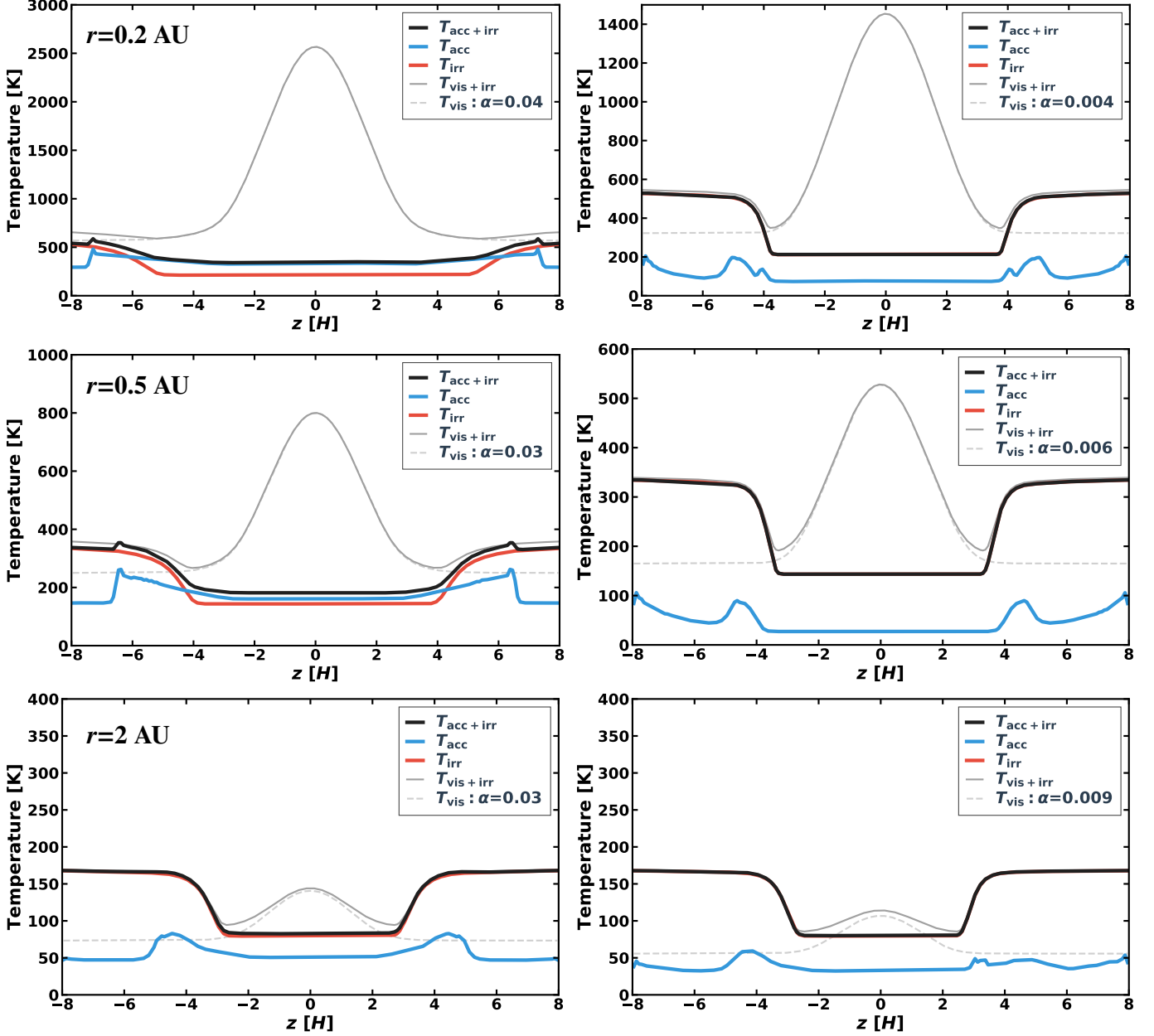


Figure 8. Same as Figure 5, but for runs with  $r = 0.2, 0.5,$  and  $2$  AU (from top to bottom).

(e.g., Chiang & Goldreich 1997). Figure 9 compares the vertical profiles of the stress and accretion heating rates from the fiducial runs with the two different prescribed temperatures.<sup>3</sup> It shows that in normalized units, the heating rate in this case reduced by a factor of two. This

<sup>3</sup> In this simulation run, the signs of the horizontal fields  $B_x$  and  $B_y$  are opposite to those in the original fiducial run. However, this has no physical significance because the equations governing the local shearing box are invariant under the transformation  $(x, y) \rightarrow (-x, -y)$ . The polarity of the horizontal field in the saturation state is randomly determined depending on the initial perturbations.

difference mainly comes from the temperature dependence on the diffusivities. Since the posterior temperature given by Equation (10) scales with the heating rate as weakly as  $q^{1/4}$ , a variation of the prior temperature only weakly affects the posterior temperature.

### 5.3. Impacts of Inefficient Accretion Heating on Planet Formation

Conventionally, the temperature profiles of PPDs in planet formation studies are obtained by adopting a simple viscous accretion disk model, similar to our constant- $\alpha$  model. In the more realistic situation of wind-driven accretion with a largely laminar disk, our results indi-

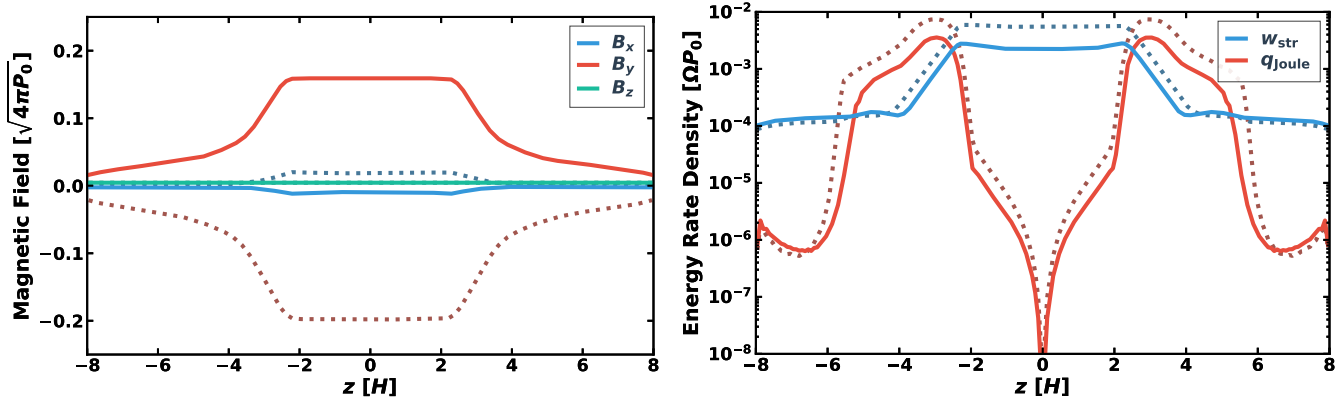


**Figure 9.** Same as the top panels of Figure 1, but for the run with  $T = 280$  K. Dotted lines show the results of the fiducial run for comparison.

cate that accretion heating of the disk interior is much less efficient, and viscous heating models could overestimate the temperature near the midplane, where planet formation mainly proceeds. These results could have a number of implications for planet formation.

For example, one important constraint can be derived on the formation history of the solar-system rocky planets including the Earth (Oka et al. 2011; Sato et al. 2016; Morbidelli et al. 2016). The fact that the water content of the solar-system terrestrial planets is tiny implies that they formed interior to the snow line. Constant- $\alpha$  disk models infer that the inner region of the solar nebula where the terrestrial planet formed retained a temperature above the sublimation point of water ice as long as the nebular accretion rate is comparable to or above the median accretion rate of classical T-Tauri stars,  $10^{-8} M_{\odot} \text{ yr}^{-1}$  (Davis 2005; Oka et al. 2011; Bitsch et al. 2015). However, in the absence of viscous heating, the nebular temperature at heliocentric radii of  $\approx 1$  au must have fallen below the ice sublimation point as the young Sun’s luminosity decreased to the present-day solar luminosity (Kusaka et al. 1970; Chiang & Goldreich 1997; Turner et al. 2012), which likely occurred in  $\approx 1$  Myr after Sun’s formation (Turner et al. 2012; Bitsch et al. 2015). This would imply that the solar-system rocky planets either formed very early ( $\lesssim 1$  Myr), or had formed closer to the sun and subsequently migrated outward to arrive at their present-day positions. The latter scenario is consistent with a recent model of rocky planet formation invoking nebular gas dispersal due to disk winds (Ogihara et al. 2017).

Another important implication is related to the fact that the inner disk region  $R \lesssim 0.5$  AU may possess either a cold laminar state without thermal-ionization driven by disk winds, or a hot MRI-turbulent state with thermal ionization (see our earlier discussions on Figure 8). This fact suggests that the dynamics of such

innermost disk regions are complex and may exhibit state transitions depending on the history of evolution. Such complex behaviors are already hinted from MHD simulations that include different levels of thermodynamics/radiative transfer and Ohmic resistivity (Faure et al. 2014, 2015; Flock et al. 2017), and may have profound implications to planet formation (e.g., Chatterjee & Tan 2014). In addition, the rate and direction of type-I planet migration are known to sensitively depend on the thermodynamic structure of PPDs (Tanaka et al. 2002; Bitsch et al. 2015), again requiring reliable understanding of the disk heating mechanisms that we have studied.

#### 5.4. On Plasma Heating by Strong Electric Fields

We have neglected change of the ionization fraction due to strong electric fields (Inutsuka & Sano 2005; Okuzumi & Inutsuka 2015). In the case of MRI turbulence, the electric field may heat up electrons, enhance its adsorption onto grains, reduce the ionization fraction, and in turn further damp the MRI (Okuzumi & Inutsuka 2015; Mori & Okuzumi 2016; Mori et al. 2017). Much stronger electric field, on the other hand, may trigger electric discharge (known as lightning), and thereby increase of the ionization level that promotes the MRI (Inutsuka & Sano 2005; Muranushi & Inutsuka 2009). While our simulations are laminar, the layer especially where horizontal magnetic field flips may possess substantial current density, that might make the system enter this regime of non-linear Ohm’s law. This effect will be addressed in future publications.

## 6. SUMMARY AND CONCLUSION

In this work, we have investigated the temperature profiles in the inner region of PPDs, where recent studies have suggested that the weakly ionized disks are largely laminar with accretion primarily driven by magnetized disk winds. Correspondingly, accretion heating mostly

takes the form of Joule dissipation instead of viscous dissipation. To this end, we have performed quasi-1D shearing-box non-ideal MHD simulations to quantify the Joule dissipation profiles, based on which disk vertical temperature profiles are calculated. We start from analyzing accretion heating with fiducial parameters, followed by a parameter exploration. The results are summarized as follows.

- The energy dissipation due to Joule heating in PPDs is the strongest at relatively high altitudes ( $z \sim 3H$ ), as a result of poor conductivity at disk midplane. This leads to little heat accumulation in the midplane region, and hence reduced midplane temperature.
- The Joule heating profile depends on the polarity of net vertical magnetic fields threading the disk (even though the wind stress does not), due to the Hall effect. It is enhanced in the aligned ( $\mathbf{B}_0 \cdot \boldsymbol{\Omega} > 0$ ) case due to the Hall-shear instability, and is strongly reduced in the anti-aligned case.
- At a given accretion rate, Joule heating is much less efficient than viscous heating, yielding much smaller midplane temperatures especially in the inner disk regions. Varying disk surface density, radial location, magnetization and dust abundances only weakly affect the conclusions above.
- As long as the disk remains largely laminar, Joule dissipation only plays a minor-to-modest (aligned) or even negligible (anti-aligned) role compared to stellar irradiation in determining disk temperature

profiles, in standard disk models. However, an MRI-turbulent state can also be sustained in the very inner disk ( $\lesssim 0.5$  AU) where viscous dissipation raises disk temperature to trigger thermal ionization.

This study shows that accretion heating in the wind-driven accretion PPDs is much weaker than commonly assumed. It also highlights the importance of stellar irradiation rather than the accretion heating in determining PPD temperatures even in the early stages of disk evolution. More self-consistent simulations in full three dimensions are needed to better address the coupling between radiative processes and gas dynamics, which requires coupling non-ideal MHD with radiative transfer as well as non-thermal and thermal ionization physics. Meanwhile, consequences of these results to planet formation remain to be explored.

The authors thank Hubert Klahr, Oliver Glessel, Neal Turner, Hidekazu Tanaka, Shigenobu Hirose, Kengo Tomida, Kazunari Iwasaki, and Takahiro Ueda for fruitful discussion and meaningful comments. The authors also thank the anonymous referee for comments that improved the paper. This work was supported by JSPS KAKENHI Grant Number JP15H02065, JP16K17661, JP16H04081, and JP17J10129. XNB acknowledges support from Tsinghua University. Numerical computations were carried out on Cray XC30 and XC50 at Center for Computational Astrophysics, National Astronomical Observatory of Japan.

## APPENDIX

### A. TEMPERATURE STRUCTURE OF REFLECTION-ASYMMETRIC DISSIPATION PROFILE IN DISKS

We here derive the analytic expressions of the temperature profile with a general dissipation profile by solving the radiative transfer equation of thermal radiation.

We extend the derivation of [Hubeny \(1990\)](#) by taking into account the following two effects. [Hubeny \(1990\)](#) assumed that the work done by the viscous stress is locally dissipated in a Keplerian disk. However, this is no longer true in the wind-driven scenario, as we see in [Figure 1](#), which we now take into account. In addition, the stellar irradiation offers another heating source. Here, we use the rate profile  $q(z)$ , being the sum of dissipation and irradiation heating, as the energy source term

$$q = q_{\text{Joule}} + q_{\text{irr}} . \quad (\text{A1})$$

We assume that the incoming radiation from irradiation and outgoing radiation by dust thermal emission are in visible and infrared, respectively. This approach allows us to separately solve the radiation fields ([Calvet et al. 1991](#)), and here we only consider radiative transfer of radiation reemitted by dust. The second assumption in [Hubeny \(1990\)](#) is that energy source term has reflection symmetry across the midplane. However, this no longer holds when energy dissipation occurs at one side of the disk, since the flip of the toroidal magnetic field generally occurs at one side of the disk, as seen in global non-ideal MHD simulations (e.g., [Bai 2017](#)). Some of our simulations also show similar asymmetric structures.

We solve the radiative transfer equations of zeroth, first, and second moments of specific intensity  $I(z, \mu, \nu)$  of the cosine of the incident angle  $\mu$ . We define these moments as

$$\begin{pmatrix} J_\nu \\ H_\nu \\ K_\nu \end{pmatrix} \equiv \frac{1}{2} \int_{-1}^1 I(z, \mu, \nu) \begin{pmatrix} 1 \\ \mu \\ \mu^2 \end{pmatrix} d\mu . \quad (\text{A2})$$

In addition, we also define the frequency-integrated moments with its frequency  $\nu$  in the thermal wavelength, respectively:

$$\begin{pmatrix} J_{\text{th}} \\ H_{\text{th}} \\ K_{\text{th}} \end{pmatrix} \equiv \int_{\text{thermal}} \begin{pmatrix} J_\nu \\ H_\nu \\ K_\nu \end{pmatrix} d\nu . \quad (\text{A3})$$

The zeroth and first moments of the radiative transfer equation integrated over thermal wavelength are written as, respectively,

$$\frac{\partial H_{\text{th}}}{\partial z} = \rho \kappa_{B_{\text{th}}} B_{\text{P}} - \rho \kappa_{J_{\text{th}}} J_{\text{th}} , \quad (\text{A4})$$

$$\frac{\partial K_{\text{th}}}{\partial z} = -\rho \kappa_{H_{\text{th}}} H_{\text{th}} , \quad (\text{A5})$$

where  $\kappa_{J_{\text{th}}}$ ,  $\kappa_{B_{\text{th}}}$ , and  $\kappa_{H_{\text{th}}}$  are the absorption mean opacity, Planck mean opacity, and flux mean effective opacity, respectively (Mihalas 1978):

$$\kappa_{J_{\text{th}}} = J_{\text{th}}^{-1} \int_{\text{thermal}} \frac{\alpha_\nu}{\rho} J_\nu d\nu , \quad (\text{A6})$$

$$\kappa_{B_{\text{th}}} = B_{\text{P}}^{-1} \int_{\text{thermal}} \frac{\alpha_\nu}{\rho} B_\nu d\nu , \quad (\text{A7})$$

$$\kappa_{H_{\text{th}}} = H_{\text{th}}^{-1} \int_{\text{thermal}} \frac{\alpha_\nu + \sigma_\nu}{\rho} H_\nu d\nu , \quad (\text{A8})$$

where  $\alpha_\nu$  and  $\sigma_\nu$  are the coefficients of true absorption and scattering respectively, and  $B_{\text{P}} = \sigma T^4 / \pi$  is the frequency-integrated Planck function. Here, we assume that  $\kappa_{J_{\text{th}}} = \kappa_{B_{\text{th}}}$ , and both of them are equal to the Rosseland mean opacity  $\kappa_{\text{R}}$ .

The second basic equation is the energy balance between the energy absorption and the thermal radiation. The vertical gradient of the energy flux  $\mathcal{F} = 4\pi H_{\text{th}}$  of radiative transport is equal to the energy dissipation rate per unit volume. We also neglect the energy transport due to gas motion (e.g., advection and convection) for simplicity, which holds when such timescales are long compared to the timescale to establish thermodynamic equilibrium. Energy conservation is then expressed as

$$4\pi \frac{\partial H_{\text{th}}}{\partial z} = q . \quad (\text{A9})$$

To close the radiative transfer equations, we adopt the Eddington approximation, which assumes isotropic radiation field (e.g., Mihalas 1978; Rybicki & Lightman 1979), and it gives the relation

$$\frac{K_{\text{th}}(z)}{J_{\text{th}}(z)} = \frac{1}{3} . \quad (\text{A10})$$

In addition, for outgoing boundary conditions, we adopt the two stream approximation, where the outgoing radiation is characterized by

$$\frac{K_{\text{th}}(+\infty)}{J_{\text{th}}(+\infty)} = \frac{K_{\text{th}}(-\infty)}{J_{\text{th}}(-\infty)} = \frac{1}{3} , \quad (\text{A11})$$

$$\frac{H_{\text{th}}(+\infty)}{J_{\text{th}}(+\infty)} = -\frac{H_{\text{th}}(-\infty)}{J_{\text{th}}(-\infty)} = \frac{1}{\sqrt{3}} , \quad (\text{A12})$$



which are valid for the optically thick regions.

Using above assumptions, we integrate Equations (A9) and (A5) from  $z$  to  $+\infty$  to obtain

$$H_{\text{th}}(z) = H_{\text{th}}(+\infty) - \int_z^{+\infty} \frac{q}{4\pi} dz' , \quad (\text{A13})$$

$$K_{\text{th}}(z) = K_{\text{th}}(+\infty) + \int_z^{+\infty} \rho\kappa_{H_{\text{th}}} H_{\text{th}} dz' . \quad (\text{A14})$$

From these equations and the boundary conditions, we can calculate  $H_{\text{th}}(z)$  and  $K_{\text{th}}(z)$ . Using Equations (A10), (A11), and (A14), we obtain

$$J_{\text{th}}(z) = J_{\text{th}}(+\infty) + 3 \int_z^{+\infty} \rho\kappa_{H_{\text{th}}} H_{\text{th}} dz' . \quad (\text{A15})$$

Using Equations (A4), (A9), and (A15), the temperature profile is expressed as

$$\frac{\sigma T^4(z)}{\pi} = \left( 3 \int_z^{+\infty} \rho\kappa_{H_{\text{th}}} H_{\text{th}} dz' + J_{\text{th}}(+\infty) \right) + \frac{1}{\rho\kappa_{\text{R}}} \frac{q}{4\pi} , \quad (\text{A16})$$

where we have used  $B = \sigma T^4/\pi$ . Using Equation Equation (A12), the temperature profile is further expressed as

$$T(z) = \left( \frac{4\pi H_{\text{th}}(+\infty)}{\sigma} \right)^{1/4} \left( \frac{3}{4H_{\text{th}}(+\infty)} \int_z^{+\infty} \rho\kappa_{H_{\text{th}}} H_{\text{th}} dz' + \frac{\sqrt{3}}{4} + \frac{1}{4H_{\text{th}}(+\infty)\rho\kappa_{\text{R}}} \frac{q}{4\pi} \right)^{1/4} . \quad (\text{A17})$$

If  $H_{\text{th}}(+\infty)$  is known, with  $H_{\text{th}}$  given by Equation (A13), the temperature profile can be directly obtained by Equation (A17). Using Equation (A13), we see

$$H_{\text{th}}(+\infty) - H_{\text{th}}(-\infty) = \frac{\Gamma}{4\pi} , \quad (\text{A18})$$

where

$$\Gamma = \int_{-\infty}^{+\infty} q dz \quad (\text{A19})$$

is the total heating (dissipation and irradiation) rate. When the dissipation profile is symmetric, we have  $H_{\text{th}}(+\infty) = -H_{\text{th}}(-\infty) = \Gamma/8\pi$  and the derivation is complete. However, this does not necessarily hold without the reflection symmetry. In the general case, we substitute Equation (A13) into Equation (A14), and  $K_{\text{th}}(z)$  can be written as

$$K_{\text{th}}(z) = K_{\text{th}}(+\infty) + H_{\text{th}}(+\infty) \int_z^{+\infty} \rho\kappa_{H_{\text{th}}} dz' - \int_z^{+\infty} \rho\kappa_{H_{\text{th}}} \left( \int_{z'}^{+\infty} \frac{q}{4\pi} dz'' \right) dz' . \quad (\text{A20})$$

Taking  $z = -\infty$  in Equation (A20), we find  $H(+\infty)$  to be

$$H_{\text{th}}(+\infty) = \frac{1}{\tau_{H,\text{tot}}} \left( -\Delta K_{+\infty} + \int_{-\infty}^{+\infty} \rho\kappa_{H_{\text{th}}} \left( \int_{z'}^{+\infty} \frac{q}{4\pi} dz'' \right) dz' \right) , \quad (\text{A21})$$

where

$$\Delta K_{\infty} = K_{\text{th}}(+\infty) - K_{\text{th}}(-\infty) , \quad (\text{A22})$$

$$\tau_{H,\text{tot}} = \int_{-\infty}^{+\infty} \rho\kappa_{H_{\text{th}}} dz . \quad (\text{A23})$$

If  $\Delta K_{+\infty}$  is given, we can then obtain  $H_{\text{th}}(+\infty)$ . Using Equations (A11) and (A12), the sum of  $H(+\infty)$  and  $H(-\infty)$  is expressed as,

$$H_{\text{th}}(+\infty) + H_{\text{th}}(-\infty) = \sqrt{3}\Delta K_{\infty} . \quad (\text{A24})$$

Combining Equations (A24) and (A18), we eliminate  $H_{\text{th}}(-\infty)$  and obtain

$$\Delta K_{\infty} = \frac{1}{\sqrt{3}} \left( 2H_{\text{th}}(+\infty) - \frac{\Gamma}{4\pi} \right) . \quad (\text{A25})$$

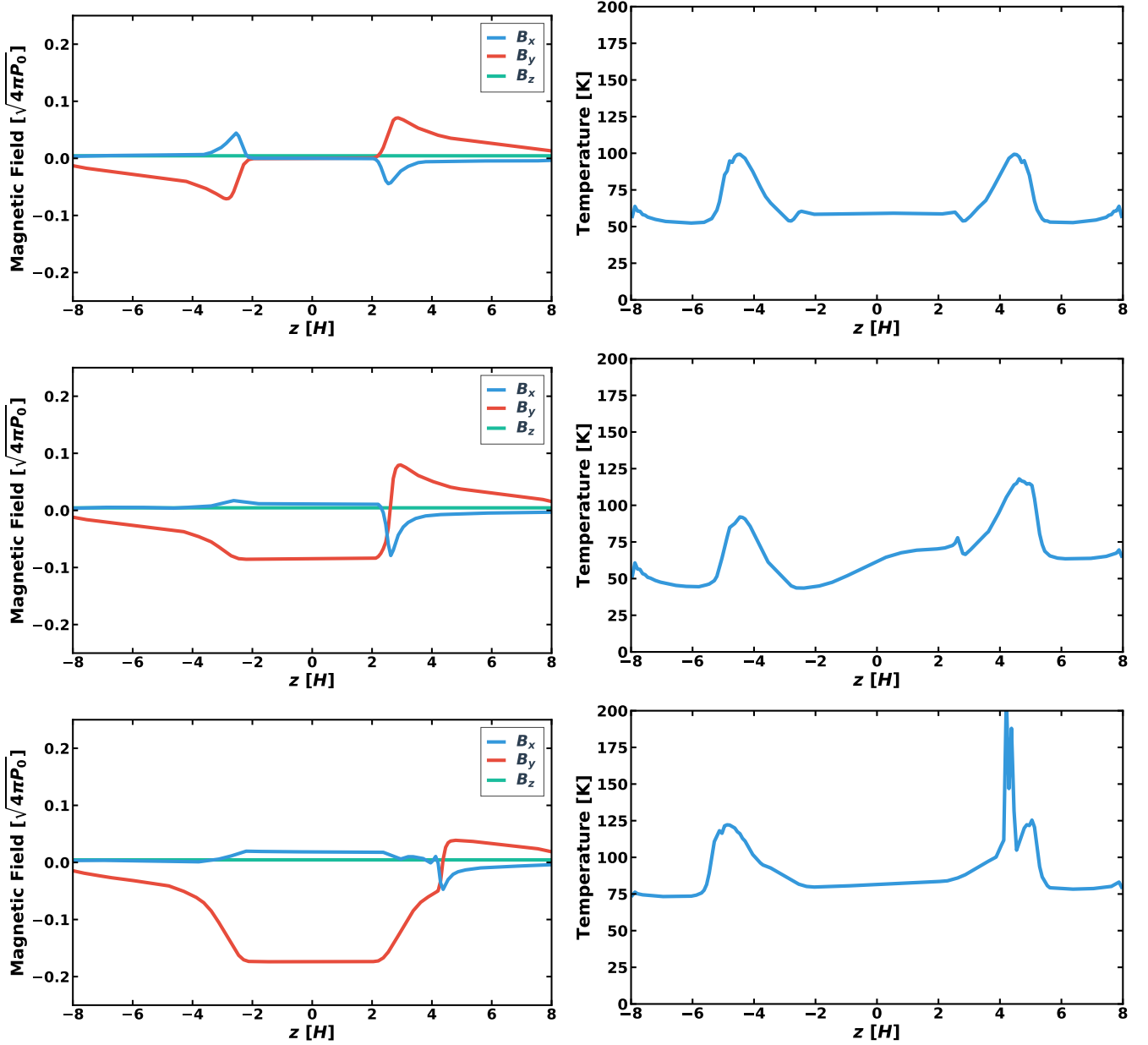


**Figure 10.** Snapshots of vertical profile of magnetic field (left) and temperature determined only by Joule heating (right) for the fiducial run at relatively early time of 4.9, 12.7, 13.9 orbits. The physical magnetic field geometry is sustained until  $\sim 12$  orbits. This field geometry is not preserved at later time as horizontal field flips to become symmetric about the midplane (due to limitation of local simulations).

Substituting Equation (A25) into Equation (A21), we obtain

$$H_{\text{th}}(+\infty) = \frac{1}{\tau_{H,\text{tot}} + 2/\sqrt{3}} \left( \frac{\Gamma}{4\sqrt{3}\pi} + \int_{-\infty}^{+\infty} \rho\kappa_{H\text{th}} \left( \int_z^{+\infty} \frac{q}{4\pi} dz' \right) dz \right). \quad (\text{A26})$$

This is the general expression for  $H(+\infty)$  that allows for asymmetric heating profiles.

Knowing  $H(+\infty)$ , we finally derive the temperature profile. Using Equations (A17) and (A26), the temperature profile is derived as

$$T(z) = T_{\text{eff}} \left( \frac{3}{4}\tau_{\text{eff}}(z) + \frac{\sqrt{3}}{4} + \frac{q}{4\rho\kappa_{\text{R}}\mathcal{F}_{+\infty}} \right)^{1/4}, \quad (\text{A27})$$

where we use the radiative flux at the upper surface  $\mathcal{F}_{+\infty} = 4\pi H_{\text{th}}(+\infty)$ , and  $T_{\text{eff}} = (\mathcal{F}_{+\infty}/\sigma)^{1/4}$  is the effective temperature observed from the upper side, and

$$\tau_{\text{eff}}(z) = \int_z^{+\infty} \rho \kappa_{\text{R}} \left( 1 - \frac{1}{\mathcal{F}_{+\infty}} \int_{z'}^{+\infty} q dz'' \right) dz' , \quad (\text{A28})$$

is the effective optical depth. Here, we further take  $\kappa_{H\text{th}} = \kappa_{B\text{th}} = \kappa_{\text{R}}$  by assuming that the scattering coefficient is much smaller than the absorption coefficient,  $\sigma_{\nu}/\alpha_{\nu} \ll 1$ . The first term in Equation (A27) expresses the effect that heat accumulation increases disk temperature. When the dissipation profile is reflection symmetric, the temperature profile reduces to that described in Hubeny (1990).

We note that the definition of effective optical depth, tracking back to its original expression in Equation (A17), represents a radiative-flux-weighted optical depth

$$\tau_{\text{eff}}(z) = \frac{1}{\mathcal{F}_{+\infty}} \int_z^{+\infty} \rho \kappa_{\text{R}} \mathcal{F}(z) dz' . \quad (\text{A29})$$

To better understand its physical meaning, we consider two extreme cases. When the all accretion energy is released at the midplane, above the midplane the radiative flux is equal to the outgoing flux  $\mathcal{F}_{+\infty}$ , and hence this value is equal to the standard optical depth  $\tau_{R,\text{tot}}/2$ . In the second case, assume all accretion energy is released at a height  $z = \pm z_{\text{heat}}$ . In the region between the heating positions above and below the midplane, the radiative flux is zero because the flux from the upper and lower sides cancels out. Correspondingly,  $\tau_{\text{eff}}(z)$  becomes

$$\tau_{\text{eff}}(z) = \begin{cases} \tau_{\text{col}}(z) & , (|z| \geq z_{\text{heat}}), \\ \tau_{\text{col}}(z_{\text{heat}}) & , (0 \leq |z| < z_{\text{heat}}), \end{cases} \quad (\text{A30})$$

where

$$\tau_{\text{col}}(z) = \int_z^{+\infty} \rho \kappa_{\text{R}} dz . \quad (\text{A31})$$

Especially, the effective optical depth  $\tau_{\text{eff}}(z = 0)$  at the midplane is simply the optical depth at  $z_{\text{heat}}$ , which can be much smaller than the actual midplane optical depth due to the weighting. Also note that the effective optical depth can even become negative at the midplane if large energy dissipation occurs at high altitude.

Finally, we consider an example with asymmetric heating profile. In doing so, we show in Figure 10 snapshots of the magnetic field profiles and the temperature profile resulting from only accretion heating together for the fiducial run with  $B_z > 0$  at an early evolution time of 5, 12.7, and 13.9 orbits. In this case, horizontal magnetic field flips at one side leaving a current sheet with strong dissipation.<sup>4</sup> We see that higher temperatures at the lower side than at the upper side, with a spike at the current sheet, with additional temperature peaks at the disk surface where vertical gradient of  $B_y$  is strong.

## B. CONSERVATION OF MECHANICAL ENERGY IN THE SIMULATIONS

To demonstrate energy conservation in our simulations, we first integrate Equation (7) over the computational domain to obtain the rate of change in the total mechanical energy per area as

$$\dot{\Psi}_{\text{mec}} = \frac{1}{L_x L_y} \frac{\partial}{\partial t} \int E_{\text{mec}} dV = W_{\text{str}} - W_{\text{out}} - \Gamma_{\text{Joule}} + W_{\text{pre}}, \quad (\text{B32})$$

where

$$W_{\text{out}} = \frac{1}{L_x L_y} \left( \int_{z=L_z/2} - \int_{z=-L_z/2} \right) F_{\text{mec}} dx dy \quad (\text{B33})$$

is the rate of energy loss through the vertical boundary (by disk winds),

$$W_{\text{str}} = \frac{3\Omega}{2L_y} \int_{x=L_x/2} \left( \rho v_x \delta v_y - \frac{B_x B_y}{4\pi} \right) dy dz \quad (\text{B34})$$

<sup>4</sup> Similar to the case discussed in Bai (2015), the system first evolves into an asymmetric profile with horizontal field flipping at a height offset from the midplane by several scale heights. This asymmetry is not long-lived owing to the limitation of local simulation, whereas it can be preserved in global simulations (Bai 2017, see their Figure 7, and further discussions in Section 5.1).

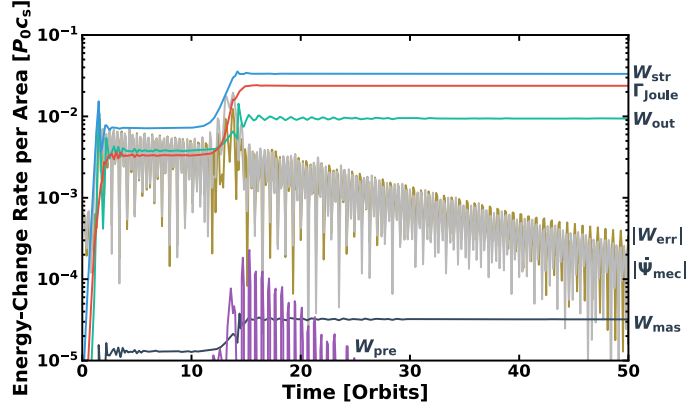


**Figure 11.** Result from the fiducial run with  $B_z > 0$ . Shown are the time variation of the time derivative of the total energy  $\dot{\Psi}_{\text{mec}}$ , the rate of work done by the Reynolds and Maxwell stress  $W_{\text{str}}$ , the rate of energy dissipation due to resistivity  $\Gamma_{\text{Joule}}$ , the rate of energy outflow through vertical boundary  $W_{\text{out}}$ , the rate of work done on the fluid by pressure  $W_{\text{pre}}$ , the rate of additional energy due to the mass conservation  $W_{\text{mas}}$ , and the rest of the energy rates  $W_{\text{err}}$  in the simulation domain, which are described in Equations (B32)–(B36).

is the rate of energy injection through the Reynolds and Maxwell stresses,

$$\Gamma_{\text{Joule}} = \frac{1}{L_x L_y} \frac{1}{c} \int \mathbf{J} \cdot \mathbf{E}' dV \quad (\text{B35})$$

is the rate of energy dissipation due to Joule heating, and

$$W_{\text{pre}} = \frac{1}{L_x L_y} \int P \nabla \cdot \mathbf{v} dV \quad (\text{B36})$$

is the work done on the fluid by pressure per unit time. The integrate of the second term in the left-hand-side of Equation (7) is eliminated because the term is a periodic quantity in the  $y$ -direction. In addition to these energy rates, we consider the other energy rates. The energy rate due to mass added for mass conservation is described by  $W_{\text{mas}}$ . We also define the rest of the energy rates as  $W_{\text{err}} = \dot{\Psi}_{\text{mec}} - (W_{\text{str}} - W_{\text{out}} - \Gamma_{\text{Joule}} + W_{\text{pre}} + W_{\text{mas}})$ .

Taking the simulation with  $B_z > 0$ , we show in Figure 11 the time evolution of each term in the equation for the mechanical energy Equation (B32). We see that despite small oscillations (presumably due to breathing mode that is leftover from initial evolution),  $W_{\text{err}}$  and  $\dot{\Psi}_{\text{mec}}$  diminishes in time, and the system converges into a steady state which is fully laminar. It also implies time average should be performed at late times, which we choose to be between 40 and 50 orbits. Over this period, we find that about 71.4% and 28.3% of  $W_{\text{str}}$  is used for the energy dissipation of Joule heating and the energy outflow by the disk wind, respectively, indicating excellent level of mechanical energy conservation (note that while Athena conserves *total energy*, there can be small truncation errors in mechanical energy conservation).

## REFERENCES

- A'Hearn, M. F., Belton, M. J. S., Delamere, W. A., et al. 2011, *Science*, 332, 1396
- Bai, X.-N. 2011, *ApJ*, 739, 50
- . 2013, *ApJ*, 772, 96
- . 2014, *ApJ*, 791, 137
- . 2015, *ApJ*, 798, 84
- . 2017, *ApJ*, 845, 75
- Bai, X.-N., & Goodman, J. 2009, *ApJ*, 701, 737
- Bai, X.-N., & Stone, J. M. 2011, *ApJ*, 736, 144
- . 2013, *ApJ*, 769, 76
- . 2017, *ApJ*, 836, 46
- Bai, X.-N., Ye, J., Goodman, J., & Yuan, F. 2016, *ApJ*, 818, 152
- Balbus, S. A., & Hawley, J. F. 1991, *ApJ*, 376, 214
- . 1998, *Reviews of Modern Physics*, 70, 1
- Balbus, S. A., & Terquem, C. 2001, *ApJ*, 552, 235
- Birnstiel, T., Ormel, C. W., & Dullemond, C. P. 2011, *A&A*, 525, A11
- Bitsch, B., Johansen, A., Lambrechts, M., & Morbidelli, A. 2015, *A&A*, 575, A28

- Calvet, N., Patino, A., Magris, G. C., & D'Alessio, P. 1991, *ApJ*, 380, 617
- Chatterjee, S., & Tan, J. C. 2014, *ApJ*, 780, 53
- Chiang, E. I., & Goldreich, P. 1997, *ApJ*, 490, 368
- Cieza, L. A., Casassus, S., Tobin, J., et al. 2016, *Nature*, 535, 258
- Davis, S. S. 2005, *ApJ*, 620, 994
- Desch, S. J. 2004, *ApJ*, 608, 509
- Desch, S. J., & Turner, N. J. 2015, *ApJ*, 811, 156
- Dzyurkevich, N., Turner, N. J., Henning, T., & Kley, W. 2013, *The Astrophysical Journal*, 765, 114
- Faure, J., Fromang, S., & Latter, H. 2014, *A&A*, 564, A22
- Faure, J., Fromang, S., Latter, H., & Meheut, H. 2015, *A&A*, 573, A132
- Flaig, M., Kley, W., & Kissmann, R. 2010, *MNRAS*, 409, 1297
- Fleming, T., & Stone, J. M. 2003, *ApJ*, 585, 908
- Flock, M., Fromang, S., Turner, N. J., & Benisty, M. 2017, *ApJ*, 835, 230
- Gammie, C. F. 1996, *ApJ*, 457, 355
- Goldreich, P., & Lynden-Bell, D. 1965, *MNRAS*, 130, 97
- Gressel, O., Turner, N. J., Nelson, R. P., & McNally, C. P. 2015, *ApJ*, 801, 84
- Grimm, S. L., Demory, B.-O., Gillon, M., et al. 2018, *A&A*, 613, A68
- Guillot, T. 2010, *A&A*, 520, A27
- Hawley, J. F., Gammie, C. F., & Balbus, S. A. 1995, *ApJ*, 440, 742
- Hayashi, C. 1981, *Progress of Theoretical Physics Supplement*, 70, 35
- Hirose, S., Krolik, J. H., & Stone, J. M. 2006, *ApJ*, 640, 901
- Hirose, S., & Turner, N. J. 2011, *ApJL*, 732, L30
- Hubeny, I. 1990, *ApJ*, 351, 632
- Inutsuka, S., & Sano, T. 2005, *ApJL*, 628, L155
- Jin, L. 1996, *ApJ*, 457, 798
- Kataoka, A., Tanaka, H., Okuzumi, S., & Wada, K. 2013, *A&A*, 557, L4
- Kunz, M. W. 2008, *MNRAS*, 385, 1494
- Kunz, M. W., & Balbus, S. A. 2004, *MNRAS*, 348, 355
- Kusaka, T., Nakano, T., & Hayashi, C. 1970, *Progress of Theoretical Physics*, 44, 1580
- Lesur, G., Kunz, M. W., & Fromang, S. 2014, *A&A*, 566, A56
- Lodders, K. 2003, *ApJ*, 591, 1220
- Masset, F. 2000, *A&AS*, 141, 165
- Mihalas, D. 1978, *Stellar atmospheres /2nd edition/* (Oxford University Press)
- Morbidelli, A., Bitsch, B., Crida, A., et al. 2016, *Icarus*, 267, 368
- Mori, S., Muranushi, T., Okuzumi, S., & Inutsuka, S.-i. 2017, *ApJ*, 849, 86
- Mori, S., & Okuzumi, S. 2016, *ApJ*, 817, 52
- Muranushi, T., & Inutsuka, S.-i. 2009, *ApJL*, 691, L24
- Ogihara, M., Kokubo, E., Suzuki, T. K., Morbidelli, A., & Crida, A. 2017, *A&A*, 608, A74
- Oka, A., Nakamoto, T., & Ida, S. 2011, *ApJ*, 738, 141
- Okuzumi, S. 2009, *ApJ*, 698, 1122
- Okuzumi, S., & Inutsuka, S.-i. 2015, *ApJ*, 800, 47
- Okuzumi, S., Tanaka, H., Kobayashi, H., & Wada, K. 2012, *ApJ*, 752, 106
- Ormel, C. W., & Okuzumi, S. 2013, *ApJ*, 771, 44
- Perez-Becker, D., & Chiang, E. 2011, *ApJ*, 735, 8
- Rybicki, G. B., & Lightman, A. P. 1979, *Radiative processes in astrophysics* (Wiley)
- Sano, T., Miyama, S. M., Umebayashi, T., & Nakano, T. 2000, *ApJ*, 543, 486
- Sano, T., & Stone, J. M. 2002a, *ApJ*, 570, 314
- . 2002b, *ApJ*, 577, 534
- Sato, T., Okuzumi, S., & Ida, S. 2016, *A&A*, 589, A15
- Shakura, N. I., & Sunyaev, R. A. 1973, *A&A*, 24, 337
- Simon, J. B., Lesur, G., Kunz, M. W., & Armitage, P. J. 2015, *MNRAS*, 454, 1117
- Stone, J. M., & Gardiner, T. A. 2010, *ApJS*, 189, 142
- Stone, J. M., Gardiner, T. A., Teuben, P., Hawley, J. F., & Simon, J. B. 2008, *ApJS*, 178, 137
- Tanaka, H., Takeuchi, T., & Ward, W. R. 2002, *ApJ*, 565, 1257
- Tsukamoto, Y., Iwasaki, K., Okuzumi, S., Machida, M. N., & Inutsuka, S. 2015, *ApJL*, 810, L26
- Turner, N. J., Choukroun, M., Castillo-Rogez, J., & Bryden, G. 2012, *ApJ*, 748, 92
- Umebayashi, T., & Nakano, T. 1981, *PASJ*, 33, 617
- Wada, K., Tanaka, H., Suyama, T., Kimura, H., & Yamamoto, T. 2009, *ApJ*, 702, 1490
- Wardle, M. 1999, *MNRAS*, 307, 849
- . 2007, *Ap&SS*, 311, 35
- Weidenschilling, S. J. 1977, *MNRAS*, 180, 57
- Xu, R., & Bai, X.-N. 2016, *ApJ*, 819, 68